

# Investigation of Minimum RVE Size for CFRP Laminates: HFGMC and PDA Framework

Mohini L. Kale

A Thesis Submitted to

Indian Institute of Technology Hyderabad

In Partial Fulfillment of the Requirements for

The Degree of Master of Technology



भारतीय प्रौद्योगिकी संस्थान हैदराबाद  
Indian Institute of Technology Hyderabad

Department Of Mechanical and Aerospace Engineering

June 2016

---

## Declaration

I declare that this written submission represents my ideas in my own words, and where ideas and words of others have been included, I have adequately cited and referenced the original sources. I also declare that I have adhered to all principles of academic honesty and integrity and have not misinterpreted or fabricated or falsified any idea/data/fact/source in my submission. I understand that any violation of the above will be a cause for disciplinary action by the Institute and can also evoke penal action from the sources that have thus not been properly cited, or from whom proper permission has not been taken when needed.



(Signature)

Mohini L. Kale

(Student Name)


ME14MTECH11029

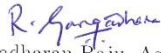
(Roll No.)


## Approval Sheet

This thesis entitled "Investigation of Minimum RVE Size for CFRP Laminates: HFGMC and PDA Framework" by Mohini L Kale is approved for the degree of Master of Technology (MTech) from Indian Institute of Technology, Hyderabad.

  
Dr. Viswanath Chinthapenta, Assistant professor  
Adviser  
Dept. of Mechanical and Aerospace Engineering  
IITH

  
Dr. Syed, Assistant professor  
Examiner  
Dept. of Mechanical and Aerospace Engineering  
IITH

  
Dr. Gangadharan Raju, Assistant professor  
Examiner  
Dept. of Mechanical and Aerospace Engineering  
IITH

  
Dr. S. Suriya Prakash, Associate professor  
Chairman  
Dept. of Civil Engineering  
IITH

## Acknowledgements

I would like to thank my thesis adviser, Dr. Viswanath Chinthapenta for his continuous support, encouragement and excellent guidance throughout the project work and thesis writing. This work could not have been completed without his efforts.

I would also like to thank my classmates and friends at IIT Hyderabad for their help and continuous support during completion of my MTech degree. I express my special thanks to Mr. Yagnik Kalaria (former student of IIT Hyderabad) for his genuine support during my research work.

Finally, I must express my gratitude towards my family for continuous encouragement throughout my study.

*To my family ...*

# Abstract

Present study focuses on finding the minimum representative volume element (RVE) size for CFRP laminate using progressive damage modeling (PDM) framework. High fidelity generalized method of cells (HFGMC) has been used in the first step of PDM for stress analysis. To interpret damage initiation and propagation in the CFRP laminate, multi-continuum theory (MCT) has been employed with sudden material property degradation rule. RVE is a smallest component of the composite material over which average macroscopic properties can be assumed constant as well as macroscopic failure theories can be easily applied. Therefore, to capture the minimum RVE size, RVE element has been studied by varying diameter of the fiber ( $D$ ) to RVE size ( $H$ ) ratio. Minimum RVE size is obtained for the CFRP laminate at  $D/H = 0.4$ .

The stiffness properties calculated using HFGMC method are validated with analytical results estimated using Halpin-Tsai model as well as experimental results obtained using digital image correlation technique available in literature. It is observed that CFRP laminate shows transversely isotropic nature till damage initiation point. After which, it loses its symmetry. The stress-strain curve is also generated for CFRP laminate for unidirectional loading.

# Contents

<b>Declaration</b>	<b>i</b>
<b>Approval Sheet</b>	<b>ii</b>
<b>Acknowledgements</b>	<b>iii</b>
<b>Abstract</b>	<b>v</b>
<b>List of Figures</b>	<b>ix</b>
<b>List of Tables</b>	<b>x</b>
<b>Nomenclature</b>	<b>xii</b>
<b>1 Micromechanical Analysis of Composite Materials</b>	<b>1</b>
1.1 Overview of Composite Materials . . . . .	1
1.2 Damage Mechanics in Composite Materials . . . . .	3
1.3 Analysis of Composite Materials . . . . .	4
1.3.1 Macro-mechanical analysis: . . . . .	4
1.3.2 Micro-mechanical analysis: . . . . .	5
1.4 Analytical and Semi-analytical Methods for Micro-mechanical Analysis . . . . .	5
1.5 Numerical Methods for Micro-mechanical Analysis . . . . .	7
1.6 Introduction to Representative Volume Element (RVE) . . . . .	8
1.7 Literature Review . . . . .	8
1.8 Motivation, Scope and Objectives . . . . .	10
1.9 Thesis Layout . . . . .	11

---

<b>2</b>	<b>Stress Analysis Using High Fidelity Generalized Method of Cells</b>	<b>12</b>
2.1	General Formulation . . . . .	12
2.2	Equilibrium and Continuity Conditions: . . . . .	15
2.2.1	Equilibrium condition: . . . . .	15
2.2.2	Displacement continuity conditions: . . . . .	16
2.2.3	Traction boundary condition:- . . . . .	16
2.3	Boundary Conditions Applied on Repeating Unit Cell (RUC):- . . . . .	17
2.4	Global Residual Vector . . . . .	18
2.5	Newton - Raphson Iteration Scheme . . . . .	21
2.6	Summary . . . . .	23
<b>3</b>	<b>Progressive Damage Modeling of Composites</b>	<b>24</b>
3.1	Introduction to PDM . . . . .	24
3.2	Damage Detection . . . . .	25
3.2.1	Multi-continuum theory . . . . .	26
3.3	Damage Modeling . . . . .	28
3.3.1	Sudden material property degradation rule (MPDM) . . . . .	28
3.4	Summary . . . . .	29
<b>4</b>	<b>Prediction of Failure and Stress-strain Behavior of CFRP Laminate</b>	<b>30</b>
4.1	Input Parameters Required for PDM of CFRP Laminate . . . . .	30
4.2	Numerical Implementation . . . . .	31
4.3	Validation of Numerical Results using Experimental and Analytical Approach . . . . .	34
4.3.1	Analytical approach . . . . .	34
4.4	Comparison between Numerical and FEM Results . . . . .	35
4.4.1	Finite element modeling . . . . .	36
4.5	Stress-strain Behavior of CFRP Composite Laminate . . . . .	37
4.6	Stress-strain components in the CFRP laminate . . . . .	39
4.7	Damage Propagation in CFRP Laminate . . . . .	40
4.8	Stiffness Properties of CFRP Composite Laminate . . . . .	42
4.9	Summary . . . . .	45
<b>5</b>	<b>RVE Interaction Effect</b>	<b>46</b>
5.1	Fiber Interaction Effect . . . . .	47



---

5.2	Different Types of RVE Configurations . . . . .	48
5.2.1	1I RVE Configuration: . . . . .	49
5.2.2	2IT RVE configuration: . . . . .	52
5.2.3	2IL RVE configuration . . . . .	54
5.2.4	2I RVE configuration . . . . .	56
5.3	Comparison Between Different RUC Configurations . . . . .	57
5.4	Summary . . . . .	59
<b>6</b>	<b>Conclusions and Scope of Future Work</b>	<b>60</b>
6.1	Conclusions . . . . .	60
6.2	Scope for Future Work . . . . .	60
	<b>Appendices</b>	<b>62</b>
<b>A</b>	<b>High Fidelity Generalized Method of Cells (HFGMC)</b>	<b>63</b>
A.1	Equation of stress . . . . .	63
A.2	Displacement and traction continuity conditions . . . . .	64
A.3	Residual vector . . . . .	67
	<b>References</b>	<b>69</b>

# List of Figures

1.1	Representative micro-structure of polymer matrix composite material. . . . .	1
1.2	Percentage distribution of composites in various applications [1] . . . . .	2
1.3	Failure modes observed in the CFRP composite material . . . . .	4
2.1	Micro-structure of CFRP composite with $(x_2, x_3)$ global co-ordinate system . . . . .	13
2.2	Repeating unit cell . . . . .	13
2.3	Additional constraint . . . . .	17
2.4	Global system of equations . . . . .	19
2.5	Stress integration points on the sub-cell [2] . . . . .	20
2.6	Newton Raphson iteration method [3] . . . . .	22
3.1	Steps in progressive damage modeling . . . . .	25
4.1	RUC Dimension and loading condition ( <i>all the dimensions are in mm</i> ) . . . . .	31
4.2	Flowchart for HFGMC method [2] . . . . .	33
4.3	Component of stress in fiber direction ( $\sigma_{11}$ ) . . . . .	36
4.4	Component of stress in loading direction ( $\sigma_{33}$ ) . . . . .	37
4.5	Stress-strain curve for CFRP composite . . . . .	38
4.6	Stress-strain curve for different sub-cell array . . . . .	38
4.7	Stress and strain component in $y_2$ direction . . . . .	39
4.8	Stress and strain component in $y_3$ direction . . . . .	40
4.9	Stress and strain component in 2-3 direction . . . . .	40
4.10	Damage propagation in CFRP composite material with increasing strain . . . . .	41
4.11	Volume fraction of damage with increasing strain . . . . .	42
4.12	Properties of CFRP composite with increasing applied strain . . . . .	43
4.13	Comparison between $E_{22}$ and $E_{33}$ properties . . . . .	44

5.1	Micro-structure of CFRP composite	46
5.2	Repeating unit cell element in $(y_2, y_3)$ co-ordinate system	47
5.3	Different RVE configurations	47
5.4	Fiber interaction effect in different RVE configurations	48
5.5	Volume fraction of fiber vs $(D/H)$	49
5.6	Micro-structure for different $(D/H)$ ratios for 1I RVE configuration	50
5.7	Variation in the stiffness properties with increasing $(D/H)$ ratio for 1I RVE configuration	51
5.8	Micro-structure for different $(D/H)$ ratios for 2IT RVE configuration	52
5.9	Variation in the stiffness properties with increasing $(D/H)$ ratio for 2IT RVE configuration	53
5.10	Micro-structure of 2IL RVE configuration for different $(D/H)$ ratios	54
5.11	Variation in the stiffness properties with increasing $(D/H)$ ratio for 2IL RVE configuration	55
5.12	Micro-structure for different $(D/H)$ ratios for 2I RVE configuration	56
5.13	Variation in the stiffness properties with increasing $(D/H)$ ratio for 2I RVE configuration	57
5.14	Longitudinal elastic modulus ( $E_{11}$ ) for different RVE configurations	58
5.15	Transverse elastic modulus ( $E_{22}$ ) and shear modulus ( $G_{12}$ ) for different RVE configurations	58
A.1	Sub-cell	64
A.2	Integration points on sub-cell	67

# List of Tables

1.1	Strength to density and stiffness to density ratios for various fiber materials [4] . . . . .	3
3.1	Degradation rules for various modes of failure . . . . .	29
4.1	Properties of fiber and matrix material [5] . . . . .	30
4.2	Comparison between numerical,experimental and analytical results . . . . .	35
5.1	Dimensions of 1I RVE configuration for different ( $D/H$ ) ratio (all the dimensions are in $\mu m$ ) . . . . .	50
5.2	Dimensions of 2IT RVE configuration for different ( $D/H$ ) ratio (all the dimensions are in $\mu m$ ) . . . . .	52
5.3	Dimensions of 2IL RVE configuration for different ( $D/H$ ) ratio (all the dimensions are in $\mu m$ ) . . . . .	54
5.4	Dimensions of 2I RVE configuration for different ( $D/H$ ) ratio (all the dimensions are in $\mu m$ ) . . . . .	56

# Nomenclature

Symbol	Description
1	Longitudinal or fiber direction
2	Transverse direction
3	Loading direction
$E_{11}$	Modulus in the fiber ( $x_1$ ) direction
$E_{22}$	Modulus in the ( $x_2$ ) direction
$E_{33}$	Modulus in the ( $x_3$ ) direction
$G_{12}$	In-plane shear modulus
$G_{23}$	Out of plane shear modulus
$G_{13}$	Out of plane shear modulus
$V_f$	Volume fraction of fiber
$N_\beta$	Number of sub-cells in $y_2$ direction
$N_\gamma$	Number of sub-cells in $y_3$ direction
$u^{(\beta\gamma)}$	Displacement of ( $\beta\gamma$ ) sub-cell
$\bar{\epsilon}$	Average strain for sub-cell
$W_{(mn)}^{(\beta\gamma)}$	Displacement gradient micro-variables for ( $\beta\gamma$ ) sub-cell
$H$	Height of RVE
$L$	Length of RVE
$h_\beta$	Height of the sub-cell
$l_\gamma$	Length of sub-cell
$(x_1, x_2, x_3)$	Global co-ordinate system for CFRP laminate
$(y_1, y_2, y_3)$	Local co-ordinate system for RUC
$(y_2^{(\beta)}, y_3^{(\gamma)})$	Local-co-ordinate system for sub-cell ( $\beta\gamma$ )

---

$\epsilon^{(\beta\gamma)}$	Total strain in sub-cell ( $\beta\gamma$ )
$\sigma^{(\beta\gamma)}$	Total stress in sub-cell ( $\beta\gamma$ )
$C^{(\beta\gamma)}$	Constitutive stiffness matrix for sub-cell ( $\beta\gamma$ )
$C_{eff}$	Effective stiffness matrix for RUC element
$T_G$	Global stiffness matrix
$J$	Jacobian matrix
$R_{Global}$	Global residual vector

# Chapter 1

## Micromechanical Analysis of Composite Materials

### 1.1 Overview of Composite Materials

Nowadays, composite materials are an essential part of an aerospace and construction industries. Aircraft components like rotor blades, spoilers, propellers etc are made up of composite materials. Composites are formed by combining two or more distinct constituents at a microscopic level. Amongst all we focus on polymer matrix composites which are reinforced using Fibers. These are generally constructed using fiber and matrix material as shown in Figure 1.1. In which, fiber material provides the high strength and stiffness to the composites while the matrix material holds the reinforced fiber elements together and transfers the load. Reinforcement of the fiber material can be of different forms like particles, long or short fibers, whiskers, etc. The main advantage of a composite material is that it shows the best qualities of its constituents and some qualities that neither of the constituents possesses.

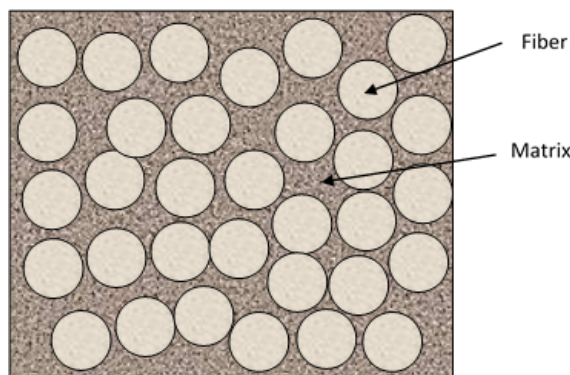


Figure 1.1: Representative micro-structure of polymer matrix composite material.

In general, composites are famous for their low weight and high strength properties [4]. They also exhibit enhanced stiffness, corrosion and wear resistance, fatigue life, strength, weight, thermal conductivity, thermal insulation etc over their constituents. However, for a given composite material and its functionality, selected material properties needs to be only tailored as per the requirements of targeted application. Hence, the intention of creating composites is to tailor the material with the enhanced required characteristics to perform the intended task. On account of their enhanced properties, composites are highly used in various engineering applications. Composite materials are generally used in various industries such as marine, aerospace, automobile, electronics, boilers, safety devices, etc. Figure 1.2 shows the percentage distribution of composites in above mentioned applications in which, 31% of composites are used in automotive applications, 26% in the construction industry, 12%, 10% and 8% composites are used in electronics, marine and appliances respectively. Amongst all industrial usage of composites in automobile industries their usage stands quite high.

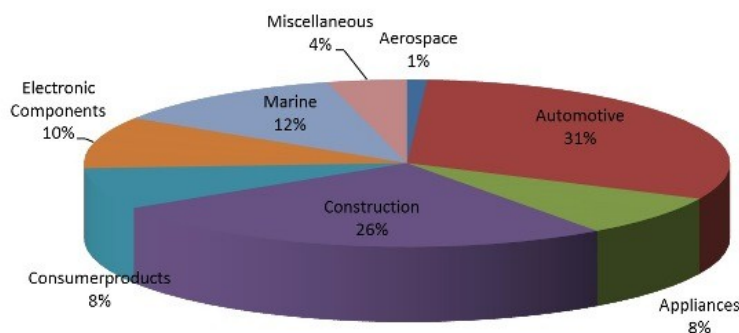


Figure 1.2: Percentage distribution of composites in various applications [1]

Composites are classified into: fibrous, particulate, and laminated composites. Fibrous composites consist of long fiber reinforcement into the matrix material whereas, in laminated composites, layers of different materials are stacked on each other. While the particles of the fiber material are scattered inside the matrix in particulate composites. Amongst above, fibrous composites are chosen for further study as it uses long fibers having greater stiffness and strength properties compared to the same composite material in the bulk form [4]. Fibrous composites can be made from different types of fiber materials. Some of the common fiber materials and their strength to density and stiffness to density ratios are described in the Table 1.1. It can be observed from the values given in the Table 1.1 that Glass fibers exhibits greater strength to density ratio as shown in the Tab. 1.1, however their stiffness to density ratio is lower than the carbon and graphite fiber. Carbon fibers are relatively expensive as compared to the glass fibers but are still preferred as they have high strength, stiffness, low weight



Table 1.1: Strength to density and stiffness to density ratios for various fiber materials [4]

Material of fiber	Strength to density ratio ( $Km$ )	Stiffness to density ratio ( $Mm$ )
Aluminium	24	2.8
Titanium	41	2.5
Steel	54	2.7
E-glass	136	2.9
S-glass	197	3.5
Carbon	123	14
Graphite	123	18

and high corrosion resistance [6]. Therefore, carbon fiber is selected for further analysis in this study. Further, polymeric matrix is chosen in this analysis.

## 1.2 Damage Mechanics in Composite Materials

Damage mechanics in the composite materials is complex problem as it consists multi-phase materials. Therefore, it has challenged many scientists from past few decades. Generally, composite materials are heterogeneous and anisotropic in nature at microscopic level [3, 4] as they are made up of fibers embedded in a polymer matrix. In majority cases, failure in composite material starts from some internal crack point and propagates as time passes. Once the failure propagates, different types of failure modes are observed in the composites like fiber rupture, matrix cracking, debonding, delamination, etc.

Matrix cracking as shown in the Figure 1.3a is the most commonly observed failure mode in the fiber reinforced composites due to overloading. Failure of matrix material due to loading in the direction perpendicular to matrix material is considered as a transverse matrix cracking. Whereas, failure of matrix material due to the loading in the matrix direction is called as longitudinal matrix cracking. Generally, failure initiates at the voids and propagates through the matrix material and reaches to the fiber which causes fiber-matrix debonding as shown in Figure 1.3b. Fiber matrix debonding is also caused by lack of adhesion between the fiber and matrix material.

De-lamination can be seen at the interface between the different layers of the laminate as shown in Figure 1.3c. Generally, delamination initiate from cracks in the matrix which grows towards the inter-laminar layer. Under certain conditions, delamination can grow when subjected to repeated loading condition and causes the failure when subsequently loaded in compression. Likewise, fiber fracture is

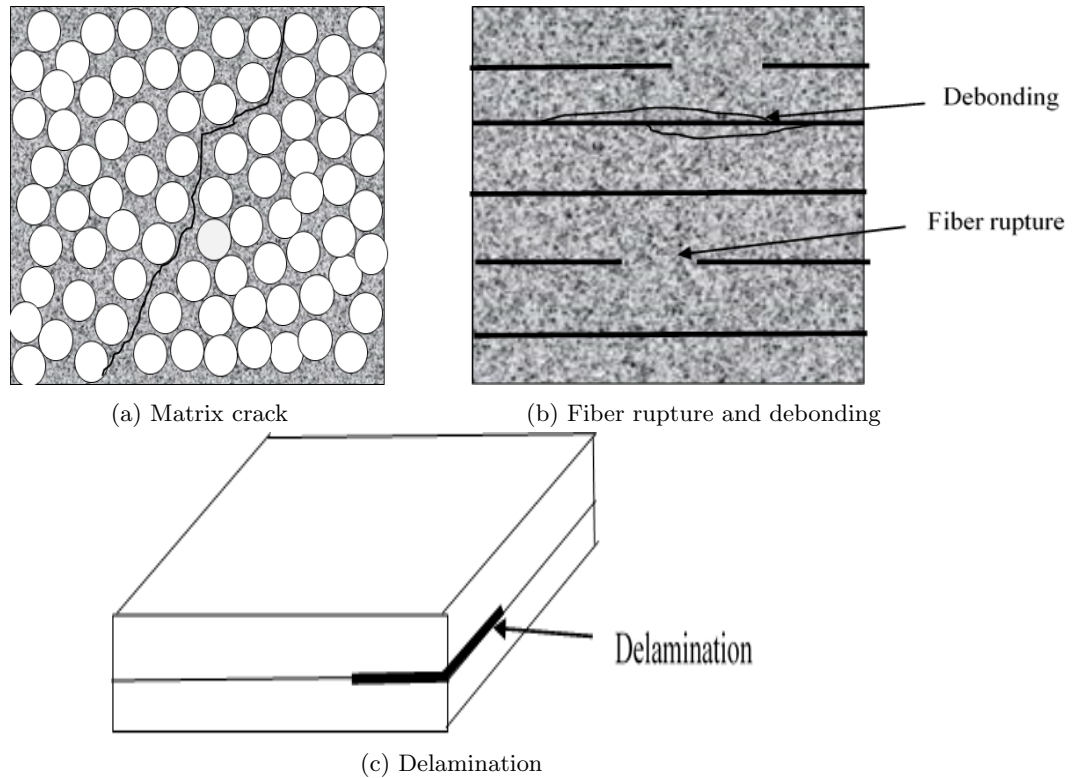


Figure 1.3: Failure modes observed in the CFRP composite material

shown in Figure 1.3b can be caused due to tensile or compressive loading in the fiber direction. Before the macroscopic failure of composite, several microscopic failures are observed. Therefore, to capture the failure modes shown in Figure 1.3, detailed analysis of CFRP composite laminate is essential.

## 1.3 Analysis of Composite Materials

Composites are heterogeneous and anisotropic in nature, therefore, they show non-local and non-linear mechanical behavior [2, 7]. Because of their orthotropic nature, shear coupling effect can also be observed [3]. To examine all these effects, detailed microscopic analysis of CFRP laminate is unavoidable. There are two main approaches present in the literature which can be used for the analysis of composites [4]:

### 1.3.1 Macro-mechanical analysis:

In this approach, composite materials are assumed as homogeneous in nature at macro-level and average material properties of the component are considered. However, micro-mechanical approach is

preferred over it due to following reasons:

- Micromechanics approach enables to capture physics of the deformation and damage at more fundamental scale [8].
- Micromechanics approach captures varying local non-proportional, multi-axial stress and strain states [9, 10].
- In micro mechanics, simpler isotropic constituent constitutive models are utilized [4].
- Simpler and more fundamental failure criteria are sufficient for micro-mechanical analysis of composite materials.
- Microstructural effects can be explicitly captured using micro-mechanics [11, 12].

### 1.3.2 Micro-mechanical analysis:

In this analysis, behavior of constituent material has been studied at micro level and interaction effect of constituent materials is also considered. The presence of long unidirectional fibers reinforced into the matrix material causes anisotropy in the composite structure. Further, size of the individual constituents such as fibers, matrix, voids, interfaces, short cracks plays significant role in component strength. Therefore, to capture the size effects and characteristic material length, accurate modeling of non-local behavior of the composites at micro-scale is essential [3, 10]. This non-local behavior significantly depends on the deformation and damage progression at micro-scale. To capture the size effect, there are three main approaches already discussed in the literature which are Cosserat deformations/ Micro-polar elasticity [9], gradient theories [13] and non-local theories [8, 10]. Among these three approaches, first two require the concept of generalized forces and balance laws but physical understanding of these laws is tricky. Therefore, non-local theory is preferred as it does not require the concept of generalized balance laws.

## 1.4 Analytical and Semi-analytical Methods for Micro-mechanical Analysis

There are different analytical and semi-analytical methods which can be used for micro-mechanical analysis of composites:

1. Voigt and Reuss Method [7, 14, 15]:

Voigt and Reuss have studied the micro-structure of composites in which fiber material particles are scattered in a matrix element. They have not considered particle interaction effect.

Therefore, it becomes a problem of single inclusion immersed in an infinite domain of matrix hence due to the assumption of non-interacting particles, analysis leads to the unreliable results. These results are unreliable especially in the case of randomly dispersed fiber particles into the matrix material.

2. Self-Consistent Method [16, 17]:

This method is an improved version of the Voigt and Reuss method. The main idea of this analysis is to consider the particle interaction effect. This method enables to produce the effective shear and bulk responses for inclusions having volume fraction equals to 50 and greater than that but this method produces infinite effective shear response for volume fraction greater than 40% and infinite effective bulk response for any volume fraction for rigid inclusions so for avoiding this problem, the generalized self-consistent method is used in which the particle is encased in a shell of matrix material which is surrounded by an effective medium.

3. Hashin-Shtrikman Bounds [7, 18, 19, 20]:

Hashin-Shtrikman bounds method considers the bound for material properties of the composites. This method is only valid for the composites having infinite body, isotropic microstructure and the materials which show an isotropic effective response. The bounds for the material properties are sensitive to the size of the sample. This method does not give accurate results for micromechanical analysis of composites as they generally exhibit orthotropic micro-structure.

4. Mori-Tanaka Method [3, 21]:

This method is based on an averaging scheme which is used to model the elastic and plastic response of the composites. In this method, properties of the matrix material are used to compute the Eshelby tensor. This method shows good agreement for less concentration of particles in particulate composites when compared with the experimental and finite elemental results. For fibrous composites, it fails to consider the effect of plastic strain under transverse loading condition. Therefore, this method is not suitable for CFRP composites.

All the analytical and semi-analytical methods which are discussed above tries to capture the size effects but they are strictly valid only when a body is assumed to be infinite and material is isotropic in nature. But composites are generally orthotropic and nonlinear in nature as well as they are finite. While recently some numerical approaches are developed which can be used for constitutive modeling of non-linear composite materials. We have restricted our focus only on non-local theories as they do not require the concept of generalized forces and micro-balance theories. The numerical approaches

are less tricky and easy to implement. Some of these numerical approaches are discussed in next section:

## 1.5 Numerical Methods for Micro-mechanical Analysis

### 1. Method of cells (MOC) [22]:

In this method, fiber reinforced composite materials are modeled as a rectangular, double periodic or triply periodic arrays in which, fibers are reinforced continuously or discontinuously. The periodic structure is called as a repeating unit cell whose properties represent entire composite structure. Each repeating unit cell is divided into four sub-cells among which, one is a fiber sub-cell and three matrix subcells. Therefore, the solution for repeating unit cell gives stresses and strains in the individual sub-cells. This approximate solution obtained is used to calculate effective macroscopic properties of the composites in an elastic and inelastic region.

### 2. Generalized method of cells (GMC) [23]:

GMC is an advancement in the method of cells. This method is capable of modeling the multi-phase composites which were not possible by using the method of cells. The Inelastic thermo-mechanical response of multi-phase composites can be captured by using this method. Modeling of various fiber architectures, porosities and damage are possible by this method. The interfacial degradation can be used to model the region around inclusions. By using this method, the composite structure can be divided into any number of sub-cells.

### 3. High Fidelity Generalized Method of Cells (HFGMC) [3, 23]:

HFGMC is developed from the generalized method of cells. It has many advantages over GMC such as higher order displacement tensor is used in HFGMC which gives more accurate results compared to the generalized method of cells since GMC has only implemented first order displacement theory. The most important advantage of HFGMC is it can capture the shear coupling effect. HFGMC has the ability to couple internal normal and shear deformations within the phases. It gives more accurate results for stresses developed in repeating unit cell (RUC) compared to previously mentioned numerical methods.

In here, high fidelity generalized method of cells has been chosen for micro-mechanical analysis of composites. It gives accurate results compared to above mentioned semi-analytical, analytical and numerical methods. Further, it has implementation simplicity in handling heterogeneous and non-linear materials [3, 23]. To find the complete mechanical behavior of composites, the study of damage

initiation and propagation is essential. In this study, progressive damage modeling (PDM) has been used to model the damage behavior of composites [24, 25, 26].

## 1.6 Introduction to Representative Volume Element (RVE)

Representative volume element is a smallest component of the composite material over which average macroscopic properties can be assumed as constant. It is the smallest volume over which macroscopic failure theories can also be applied. The overall modulus tensor which relates the stress to strain assumed constant over the RVE. Representative volume element is not necessarily same as the repeating unit cell (RUC). RVE describes the minimum volume of the material where properties of the composites are constant while RUC is a repeating periodic structure. Only in some cases, RUC gives detailed account of the properties of a composite material. In such cases, RUC can be considered as representative volume element of the material. Drugan et al. [27, 28, 29] have elaborated an analytical method based on non-local micro-mechanical analysis using Hashin-Shtrikman variational principle to find the minimum RVE size for composites. But these closed form analytical estimates are applicability is restricted to isotropic composites. However, CFRP composite generally exhibits heterogeneous and transversely isotropic nature. The analytical methods specified by Drugan et al. [27] to find the minimum RVE size for CFRP composite are not that straightforward to apply to transversely isotropic materials. Therefore, in present work, the high fidelity generalized method of cells has been used to overcome the downsides of Drugan's [27] work.

## 1.7 Literature Review

In this section we present the detailed literature review of stress analysis using HFGMC framework and progressive damage analysis in composite structures. M Paley et al. [30] have used generalized method of cells for micro-mechanical analysis of composites. In this study, RUC is divided into an arbitrary number of sub-cells to model the multiphase periodic composite material. The effective constitutive response of the elastic-viscous-plastic composite material is added in this paper. Aboudi et al. [23] studied the micro-mechanical model by using both generalized method of cells (GMC) and High fidelity generalized method of cells (HFGMC). Both the theories are applicable to thermo-elastic, viscoelastic, thermo-inelastic and electro-magneto-thermo-elastic materials. The micromechanical approach has been established in both the theories for predicting the overall behavior of multi-phase composites. GMC is able to predict the overall response of multi-phase composites however its accuracy in predicting local stress and strain fields is less in HFGMC method due to first order displacement

tensor. HFGMC consists of second-order displacement tensor which increases the accuracy in finding the inhomogeneous stress-strain fields.

Haj-Ali et al. [3] have used the high fidelity generalized method of cells to study the behavior of a nonlinear elastic, elastic-plastic and viscous-plastic constituents. HFGMC micro-mechanical modeling formulation increases the computational efficiency with usage of multi-scaling. In this analysis, a nonlinear finite elemental analysis is implemented using HFGMC formulation which helped for local-global stress analysis. Traction and displacement continuity conditions are used to derive the global set of equations. Ivancevic et al. [2] studied the micro-mechanical damage modeling in composite materials using HFGMC and failure mechanism in a heterogeneous material. Drugan and Willis [27, 28] analytically estimated the minimum representative volume element size (RVE) for an isotropic material. They showed that the leading order correction for the macroscopically homogeneous constitute requires a second order gradient of the ensemble average of strain. The high fidelity generalized method of cells also uses second order gradient of strain. Therefore, HFGMC can be implemented for constitutive modeling of composites.

Tserpes et al. [24, 31] and Shokrieh [25, 32] have studied the progressive damage modeling for CFRP composites to find the damage initiation and propagation for fatigue loading at meso scale. Tserpes et al. [24] have estimated fatigue life of CFRP laminate and its influence on initiation and propagation of edge delamination. Ubaid et al. [33] and Saurabh et al.[26] have used PDM technique to predict the damage behavior of CFRP laminate containing two holes arranged in different configurations under tensile and compressive loading respectively. Saurabh et al. [26] have considered a CFRP panel with multiple interacting holes of various configurations like 1H, 2HL, 2HT and 2HD to study the interaction effects.

There are three main steps in the PDM: stress analysis, damage detection, damage modeling. In the first step, high fidelity generalized method of cells has been used to obtain current stress state of the laminate. Aboudi et al. [22, 34] have applied the micro-mechanical theory to repeating unit cell (RUC) in which fiber is reinforced in the matrix phase. The analysis is applicable to elastic, thermo-elastic, viscoelastic, and viscous-plastic composites. The method of cells is used for this analysis so that RUC is divided into four sub-cells, out of which one consists of fiber material and other three are made up of a matrix material. The micro-mechanical analysis using MOC considers the interaction between the neighboring RUCs and sub-cells. Traction and displacement continuity conditions are imposed on an average basis and the equilibrium condition is also satisfied for each sub-cell. The effective properties of the RUC are determined using fiber-matrix properties.

P. Nali et al. [35] studied the different failure criteria in two dimensions which can be used for

damage detection in the second step of PDM. They have compared the popular failure criteria like Hashin failure criterion, LARC 03, Tsai-Wu, Tsai-Hill, maximum stress and maximum strain criterion for anisotropic materials. Plane stress condition with finite elemental analysis have been considered for checking advantages and disadvantages for different failure theories. Steven Mayes et al. [36] studied the progressive failure analysis of composite materials for uniaxial and multi-axial loading by using multi-continuum theory. Constituent-based failure is analyzed for fiber and matrix material failure by using MCT criterion. It is assumed that composite material is multi-continuum in nature and matrix and fiber material constituent stress and strain fields are estimated. Ivancevic et al. [2] has also used multi-continuum theory for damage modeling of heterogeneous composite materials. MCT is a constituent based theory. Therefore, it can be used to find the local damage state of the heterogeneous material. Therefore, the multi-continuum theory is used for finding the current damage state of the heterogeneous CFRP composite laminate. Once the damage is detected, material properties of the damaged sub-cells need to be degraded. Shokreih et al. [25, 32] has focused on two ways of degrading the material properties, sudden degradation, gradual degradation. In sudden degradation, material properties of the failed elements are directly reduced to zero. Generally, sudden material property degradation rule is preferred for static loading condition. In the case of fatigue loading, both sudden and gradual material property degradation rule are applied.

Tserpes et al. [24, 31] used sudden material property degradation rule for degrading the material properties of CFRP laminate. Material properties are degraded using sudden degradation rule for matrix tensile cracking, matrix compressive cracking, fiber tensile cracking, fiber compressive cracking, fiber matrix shear out, delamination in tension and compression. Shokreih and Lessard [25, 32] have explained both the material property degradation rules in their study. The stiffness and strength of the failed elements are reduced during progressive damage analysis using the expressions given in the paper. Sourabh et al. [26] and Ubaid et al. [33] have also used sudden material property degradation rule to carry out the PDM. Sudden material property degradation rule is chosen for further analysis as the scope of this research work considers static loading.

## 1.8 Motivation, Scope and Objectives

Drugan et al. [27, 28, 29] have established explicit constitutive equation which relates the average strain and stresses in a linear elastic composite material by using non-local micro-mechanical approach. They have used a Hashin- Shtrikman [18, 19, 20] variational formulation to derive the quantitative estimate for minimum RVE size for two-phase composites analytically But this method is applicable to only isotropic and statically uniformly distributed composites. However, composite materials are



generally heterogeneous and anisotropic in nature as well as exhibits the non-local mechanical behavior. Therefore, it is difficult if not possible to find the accurate minimum RVE size for composites using this analytical approach. Furthermore, the material would exhibit non-linear behavior once the damage initiates and its possess added complexity in analyzing analytically. Hence, to understand the interaction effect shown in Figure 5.1, it is essential to find the minimum RVE size for the composite material. Therefore, a numerical method: high fidelity of generalized method of cells has been implemented to find the minimum RVE size for CFRP laminate along with PDA. The objectives of the thesis are as follows:

- To obtain the minimum representative volume element size (RVE) for CFRP composite laminate.
- To study the stress-strain behavior of CFRP composite laminate under incremental loading with micro-structural damage.
- To capture the final failure and stiffness properties of CFRP composite laminate.

## 1.9 Thesis Layout

This research work spans over 6 chapters. Chapter 1 illustrates various micro-mechanical analysis of composite materials followed by literature review on progressive damage modeling and high fidelity generalized method of cells. In Chapter 2 discusses the implementation of stress analysis using high fidelity generalized method of cells developed by Aboudi [3] through incremental form. Chapter 3 explicitly focuses on progressive damage modeling [24] used to study the behavior of CFRP laminate. In Chapter 4 numerical implementation of progressive damage analysis of CFRP laminate are presented. In Chapter 5 the investigations on finding minimum representative volume element size of different RVE configurations are illustrated. The minimum RVE size for different RVE configurations illustrated in the Figure 5.3 is finalized based on the agreement of results of stiffness properties obtained by HFGMC method and Halpin-Tsai model within 5 % error. Finally, in Chapter 6 summary on the results and scope of future work are presented.

## Chapter 2

# Stress Analysis Using High Fidelity Generalized Method of Cells

High fidelity generalized method of cells (HFGMC) has been developed by Aboudi et al. [23] in 2004 which overcomes the drawbacks of generalized method of cells (GMC). This framework is used for micro-mechanical modeling of multi-phase composites with an enhanced computational efficiency which enables multi-scale analysis also. HFGMC is a strong analytical form which is used to solve non-linear constituent equations for estimating stress and strain components developed with finite increments of applied load. It is non-local, micro mechanical analysis method which can capture the shear coupling effect also. Therefore, for computing stress-strain variables during finite increments in the loading, high fidelity generalized method of cells has been used.

### 2.1 General Formulation

HFGMC developed by Aboudi et al. [3] has been used to find the current stress state of CFRP model. A global co-ordinate system  $(x_1, x_2, x_3)$  has been considered as shown in fig. 2.1 in which,  $x_1$  is the fiber direction. In HFGMC, a periodic microstructure of CFRP model shown in the Figure 2.1 is divided into a random number of repeating unit cells (RUC). However, RUC does not necessarily represent representative volume element (RVE) where mean-field homogenization is applied to get the homogeneous properties.

$(y_2, y_3)$  is a local co-ordinate system considered for RUC as shown in fig. 2.2a. RUC is further sub-divided into an arbitrary number of subcells.  $\beta$  and  $\gamma$  are the number of sub-cells in  $y_2$  and  $y_3$  direction respectively as shown in fig. 2.2b. A local co-ordinate system is introduced in each sub-cell with a co-ordinate system as  $(y_2^{(\beta)}, y_3^{(\gamma)})$ .

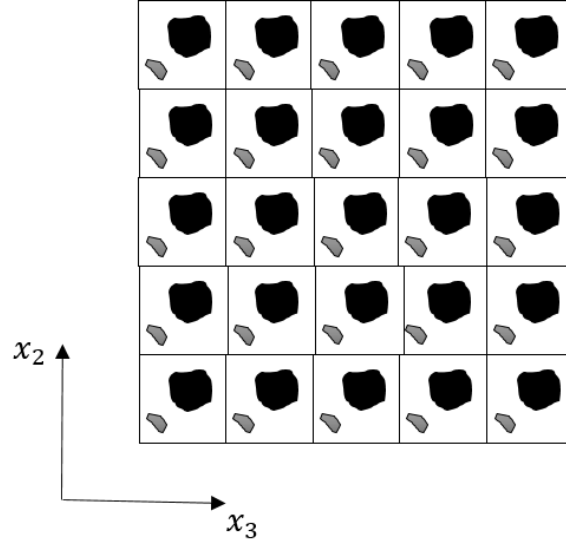


Figure 2.1: Micro-structure of CFRP composite with  $(x_2, x_3)$  global co-ordinate system

Second order displacement tensor used in the HFGMC framework is given below:

$$u^{(\beta\gamma)} = \bar{\epsilon} \cdot X + W_{(00)}^{(\beta\gamma)} + y_2^{(\beta)} W_{(10)}^{(\beta\gamma)} + y_3^{(\beta)} W_{(01)}^{(\beta\gamma)} + \frac{1}{2} \left( 3y_2^{(\beta)2} - \frac{h_\beta^2}{4} \right) W_{(20)}^{(\beta\gamma)} + \frac{1}{2} \left( 3y_3^{(\gamma)2} - \frac{l_\gamma^2}{4} \right) W_{(02)}^{(\beta\gamma)} \quad (2.1)$$

where,  $\bar{\epsilon}$  and  $W_{(mn)}^{(\beta\gamma)}$  is externally applied average strain and coefficient variable vector on volume averaged basis respectively.

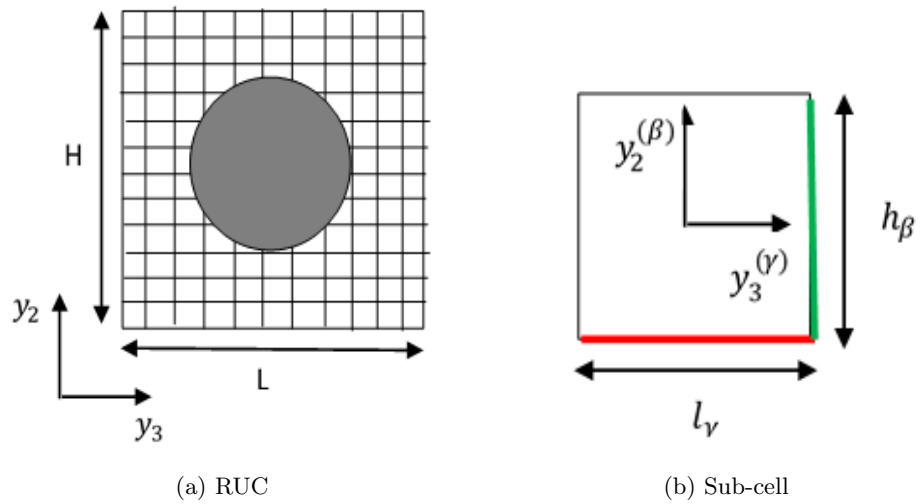


Figure 2.2: Repeating unit cell

The applied strain vector for each sub-cell is in Voigt notation,

$$\bar{\epsilon} = (\epsilon_{11}, \epsilon_{22}, \epsilon_{33}, 2\epsilon_{23}, 2\epsilon_{13}, 2\epsilon_{12}) \quad (2.2)$$

Total strain in each sub-cell can be calculated using the expression obtained by differentiating the displacement equation is given by,

$$\epsilon^{(\beta\gamma)} = \bar{\epsilon} + P_{(10)}W_{(10)}^{(\beta\gamma)} + P_{(01)}W_{(01)}^{(\beta\gamma)} + P_{(20)}W_{(20)}^{(\beta\gamma)}y_2^{(\beta)} + P_{(02)}W_{(02)}^{(\beta\gamma)}y_3^{(\gamma)} \quad (2.3)$$

After further simplification, expression for average strain in each sub-cell is obtained which is given by,

$$\bar{\epsilon}^{(\beta\gamma)} = \bar{\epsilon} + P_{(10)}W_{(10)}^{(\beta\gamma)} + P_{(01)}W_{(01)}^{(\beta\gamma)} \quad (2.4)$$

Where,  $P_{(10)}$ ,  $P_{(01)}$ ,  $P_{(02)}$  and  $P_{(20)}$  are as follows:

$$P_{(10)} = \begin{bmatrix} 0 & 0 & 0 \\ 0 & 1 & 0 \\ 0 & 0 & 0 \\ 1 & 0 & 0 \\ 0 & 0 & 0 \\ 0 & 0 & 1 \end{bmatrix} \quad P_{(01)} = \begin{bmatrix} 0 & 0 & 0 \\ 0 & 0 & 0 \\ 0 & 0 & 1 \\ 0 & 0 & 0 \\ 1 & 0 & 0 \\ 0 & 1 & 0 \end{bmatrix}$$

$$P_{(20)} = 3P_{(10)} \text{ and } P_{(02)} = 3P_{(01)}$$

The stress influence matrix  $P^{(\beta\gamma)}$  can be calculated using following expression, which is needed for calculating the effective stiffness matrix for the RUC element.

$$P^{(\beta\gamma)} = \left[ I + P_{10}\bar{D}_{(10)}^{(\beta\gamma)} + P_{01}\bar{D}_{(01)}^{(\beta\gamma)} \right] \quad (2.5)$$

where,  $I$  is a identity matrix,  $\bar{D}_{(10)}^{(\beta\gamma)}$  and  $\bar{D}_{(01)}^{(\beta\gamma)}$  can be calculated using following expression:

$$\bar{D}_{(10)}^{(\beta\gamma)} \Delta \bar{\epsilon} = \Delta W_{(10)}^{(\beta\gamma)}, \quad \bar{D}_{(01)}^{(\beta\gamma)} \Delta \bar{\epsilon} = \Delta W_{(01)}^{(\beta\gamma)}$$

The linear expansion of stress vector can be written as,

$$\sigma^{(\beta\gamma)} = \bar{\sigma}^{(\beta\gamma)} + \sigma_{(10)}^{(\beta\gamma)}y_2^{(\beta)} + \sigma_{(01)}^{(\beta\gamma)}y_3^{(\gamma)} \quad (2.6)$$

In Eq. 2.6,  $\bar{\sigma}^{(\beta\gamma)}$  is an average stress for the sub-cell and can be obtained using following mathematical equation:

$$\bar{\sigma}^{(\beta\gamma)} = C^{(\beta\gamma)}\bar{\epsilon} + C^{(\beta\gamma)}P_{(10)}W_{(10)}^{(\beta\gamma)} + C^{(\beta\gamma)}P_{(01)}W_{(01)}^{(\beta\gamma)}$$

Stress components  $\sigma_{(10)}^{(\beta\gamma)}$  and  $\sigma_{(01)}^{(\beta\gamma)}$  are calculated using,

$$\sigma_{(10)}^{(\beta\gamma)} = \frac{12}{h_\beta^2} S_{(10)}^{(\beta\gamma)}, \quad \sigma_{(01)}^{(\beta\gamma)} = \frac{12}{l_\gamma^2} S_{(01)}^{(\beta\gamma)} \quad (2.7)$$

where,  $C^{(\beta\gamma)}$  is a constitutive matrix for  $(\beta\gamma)$  sub-cell. CFRP composite material generally shows transversely isotropic nature in 2-3 plane. Therefore, constitutive matrix can be calculated using,

$$C_{(ijkl)}^{(\beta\gamma)} = \lambda \delta_{ij} \delta_{kl} + \mu (\delta_{ik} \delta_{jl} + \delta_{il} \delta_{jk}) \quad (2.8)$$

$$C^{(\beta\gamma)} = \begin{bmatrix} C_{11} & C_{12} & C_{13} & 0 & 0 & 0 \\ C_{12} & C_{22} & C_{23} & 0 & 0 & 0 \\ C_{13} & C_{23} & C_{22} & 0 & 0 & 0 \\ 0 & 0 & 0 & C_{44} & 0 & 0 \\ 0 & 0 & 0 & 0 & C_{55} & 0 \\ 0 & 0 & 0 & 0 & 0 & C_{55} \end{bmatrix} \quad (2.9)$$

For calculating  $S_{(10)}$  and  $S_{(01)}$  components, stress moment equation needed is given by,

$$S_{(mn)}^{(\beta\gamma)} = \frac{1}{h_\beta} \frac{1}{l_\gamma} \int_{-\frac{h_\beta}{2}}^{\frac{h_\beta}{2}} \int_{-\frac{l_\gamma}{2}}^{\frac{l_\gamma}{2}} \sigma^{(\beta\gamma)} y_2^{(\beta)m} y_3^{(\gamma)n} dy_2^{(\beta)} dy_3^{(\gamma)} \quad (2.10)$$

By putting the values of  $m$  and  $n$ , we can get  $S_{(mn)}^{(\beta\gamma)}$  and by using the value of  $S_{(mn)}^{(\beta\gamma)}$ , we can calculate the stress components as explained in the eq. 2.6. Derivation of stress components has been described in the section A.1.

## 2.2 Equilibrium and Continuity Conditions:

We have considered only two surfaces, surface 1 and surface 2, represented by green and red color in Figure 2.2b respectively. Symmetrical boundary conditions are assumed therefore, it is sufficient to apply continuity conditions only on two surfaces.

### 2.2.1 Equilibrium condition:

The equilibrium equation for HFGMC is [3],

$$L_2 \sigma_{(10)}^{(\beta\gamma)} + L_3 \sigma_{(01)}^{(\beta\gamma)} = 0 \quad (2.11)$$

where,  $L_2 = \text{transpose}(P_{(10)})$  and  $L_3 = \text{transpose}(P_{(01)})$

By putting the values of  $\sigma_{(10)}^{(\beta\gamma)}$  and  $\sigma_{(01)}^{(\beta\gamma)}$  obtained previously and solving eq. 2.11,

$$L_2 C^{(\beta\gamma)} P_{(20)} \Delta W_{(20)}^{(\beta\gamma)} + L_3 P_{(02)} \Delta W_{(02)}^{(\beta\gamma)} = 0 \quad (2.12)$$

This equation can be written as,

$$A_{2(20)}^{(\beta\gamma)} \Delta W_{(20)}^{(\beta\gamma)} + A_{3(02)}^{(\beta\gamma)} \Delta W_{(02)}^{(\beta\gamma)} = 0 \quad (2.13)$$

where,

$$A_{i(mm)}^{(\beta\gamma)} = L_i C^{(\beta\gamma)} P_{(mn)}, \quad A_{i(00)}^{(\beta\gamma)} = L_i C^{(\beta\gamma)}$$

### 2.2.2 Displacement continuity conditions:

The displacement continuity equation on the surface 1 as shown in the Figure 2.2b is,

$$\int_{-\frac{h_\beta}{2}}^{\frac{h_\beta}{2}} \left[ u^{(\beta\gamma)} \Big|_{y_3^{(\gamma)} = \frac{l_\gamma}{2}} - u^{(\beta\gamma_1)} \Big|_{y_3^{(\gamma_1)} = \frac{l_{\gamma_1}}{2}} \right] dy_2^{(\beta)} = 0 \quad (2.14)$$

By putting the value of displacement ( $u$ ) from eq. 2.1 in the eq. 2.14 and solving, we will get (detailed in section A.2)

$$\left[ \Delta W_{(00)}^{(\beta\gamma)} + \frac{l_\gamma}{2} \Delta W_{(01)}^{(\beta\gamma)} + \frac{l_\gamma^2}{4} \Delta W_{(02)}^{(\beta\gamma)} \right] - \left[ \Delta W_{(00)}^{(\beta\gamma_1)} - \frac{l_{\gamma_1}}{2} \Delta W_{(01)}^{(\beta\gamma_1)} + \frac{l_{\gamma_1}^2}{4} \Delta W_{(02)}^{(\beta\gamma_1)} \right] = 0 \quad (2.15)$$

This is the final expression for displacement continuity condition on surface 1. Similarly, the expression for displacement continuity condition on surface 2 is as follows:

$$\int_{-\frac{l_\gamma}{2}}^{\frac{l_\gamma}{2}} \left[ u^{(\beta\gamma)} \Big|_{y_2^{(\beta)} = \frac{h_\beta}{2}} - u^{(\beta_1\gamma)} \Big|_{y_2^{(\beta_1)} = \frac{h_{\beta_1}}{2}} \right] dy_3^{(\gamma)} = 0 \quad (2.16)$$

By solving eq. 2.16, we will get

$$\left[ \Delta W_{(00)}^{(\beta\gamma)} - \frac{h_\beta}{2} \Delta W_{(10)}^{(\beta\gamma)} + \frac{h_\beta^2}{4} \Delta W_{(20)}^{(\beta\gamma)} \right] - \left[ \Delta W_{(00)}^{(\beta_1\gamma)} + \frac{h_{\beta_1}}{2} \Delta W_{(10)}^{(\beta_1\gamma)} + \frac{h_{\beta_1}^2}{4} \Delta W_{(20)}^{(\beta_1\gamma)} \right] = 0 \quad (2.17)$$

This is the final expression for displacement boundary condition on surface 2.

### 2.2.3 Traction boundary condition:-

Now, let's consider the traction boundary condition on surface 1 as shown in the Figure 2.2b,

$$\int_{-\frac{h_\beta}{2}}^{\frac{h_\beta}{2}} \left[ L_3 \sigma^{(\beta\gamma)} \Big|_{y_3^{(\gamma)} = -\frac{l_\gamma}{2}} - L_3 \sigma^{(\beta\gamma_1)} \Big|_{y_3^{(\gamma_1)} = -\frac{l_{\gamma_1}}{2}} \right] dy_2^{(\beta)} = 0 \quad (2.18)$$

Putting eq. (2.6) in eq. (2.18) and solving, (explained in the section A.2)

$$\begin{aligned} \left[ A_{3(00)}^{(\beta\gamma_1)} - A_{3(00)}^{(\beta\gamma)} \right] \Delta \bar{\epsilon} &= \left[ A_{3(10)}^{(\beta\gamma)} \Delta W_{(10)}^{(\beta\gamma)} + A_{3(01)}^{(\beta\gamma)} \Delta W_{(01)}^{(\beta\gamma)} + \frac{l_\gamma}{2} A_{3(02)}^{(\beta\gamma)} \Delta W_{(02)}^{(\beta\gamma)} \right] \\ &\quad - \left[ A_{3(10)}^{(\beta\gamma_1)} \Delta W_{(10)}^{(\beta\gamma_1)} + A_{3(01)}^{(\beta\gamma_1)} \Delta W_{(01)}^{(\beta\gamma_1)} + \frac{l_{\gamma_1}}{2} A_{3(02)}^{(\beta\gamma_1)} \Delta W_{(02)}^{(\beta\gamma_1)} \right] \end{aligned} \quad (2.19)$$

This is the final expression for traction continuity on surface 1.

Similarly applying traction boundary conditions on the surface 2, we got the following expression:

$$\int_{-\frac{l_\gamma}{2}}^{\frac{l_\gamma}{2}} \left[ L_2 \sigma^{(\beta\gamma)} \Big|_{y_2^{(\beta)} = -\frac{h_\beta}{2}} - L_2 \sigma^{(\beta_1\gamma)} \Big|_{y_2^{(\beta_1)} = -\frac{h_{\beta_1}}{2}} \right] dy_3^{(\gamma)} = 0 \quad (2.20)$$

By solving this expression,

$$\begin{aligned} \left[ A_{2(00)}^{(\beta_1\gamma)} - A_{2(00)}^{(\beta\gamma)} \right] \Delta \bar{\epsilon} &= \left[ A_{2(10)}^{(\beta\gamma)} \Delta W_{(10)}^{(\beta\gamma)} + A_{2(01)}^{(\beta\gamma)} \Delta W_{(01)}^{(\beta\gamma)} - \frac{h_\beta}{2} A_{2(20)}^{(\beta\gamma)} \Delta W_{(20)}^{(\beta\gamma)} \right] \\ &\quad - \left[ A_{2(10)}^{(\beta_1\gamma)} \Delta W_{(10)}^{(\beta_1\gamma)} + A_{2(01)}^{(\beta_1\gamma)} \Delta W_{(01)}^{(\beta_1\gamma)} + \frac{h_{\beta_1}}{2} A_{2(20)}^{(\beta_1\gamma)} \Delta W_{(20)}^{(\beta_1\gamma)} \right] \end{aligned} \quad (2.21)$$

### 2.3 Boundary Conditions Applied on Repeating Unit Cell (RUC):-

The two sub-cells at opposite corner points A and B have been fixed as shown in the Figure 2.3a to constrain the displacement of RUC. The four edge center points  $C_1, C_2, C_3$  and  $C_4$  are fixed for both the sub cells as shown in the Figure 2.3b. Therefore, additional constrained equations needed for solving the global system of equations are given below:

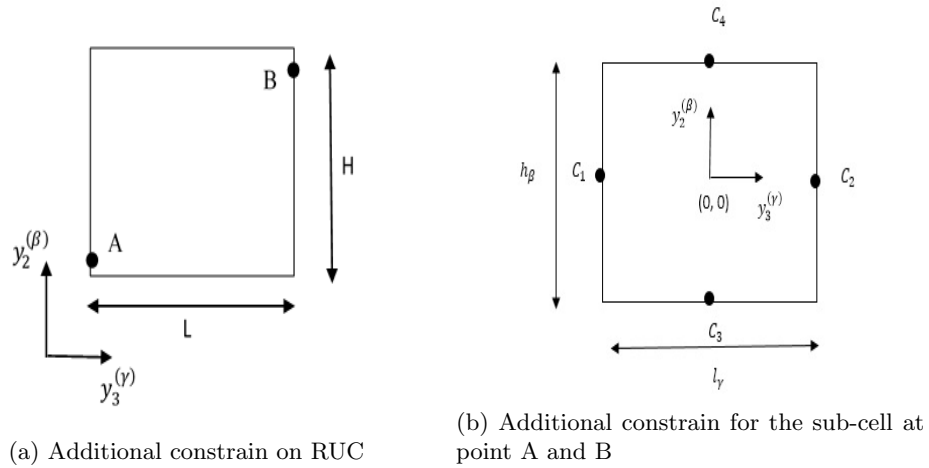


Figure 2.3: Additional constraint

$(y_2^{(\beta)}, y_3^{(\gamma)})$  is a local co-ordinate system for sub-cell. Co-ordinates of points  $C_1, C_2, C_3$  and  $C_4$  are as follows:

$$C_1 = \left( 0, -\frac{l_\gamma}{2} \right), C_2 = \left( 0, \frac{l_\gamma}{2} \right), C_3 = \left( -\frac{h_\beta}{2}, 0 \right) \text{ and } C_4 = \left( \frac{h_\beta}{2}, 0 \right)$$

Therefore, putting these values of  $C_1, C_2, C_3$  and  $C_4$  in Eq. 2.1,

$$u^{(\beta\gamma)}|_{C_1} = \left[ 0 * I_3 \quad \left(-\frac{l_\gamma}{2}\right) * I_3 \quad I_3 \quad \left(-\frac{h_{\beta^2}}{8}\right) * I_3 \quad \left(\frac{l_{\gamma^2}}{4}\right) * I_3 \right]$$

$$u^{(\beta\gamma)}|_{C_2} = \left[ 0 * I_3 \quad \left(\frac{l_\gamma}{2}\right) * I_3 \quad I_3 \quad \left(-\frac{h_{\beta^2}}{8}\right) * I_3 \quad \left(\frac{l_{\gamma^2}}{4}\right) * I_3 \right]$$

$$u^{(\beta\gamma)}|_{C_3} = \left[ \left(-\frac{h_\beta}{2}\right) * I_3 \quad 0 * I_3 \quad I_3 \quad \left(\frac{h_{\beta^2}}{4}\right) * I_3 \quad \left(-\frac{l_{\gamma^2}}{8}\right) * I_3 \right]$$

$$u^{(\beta\gamma)}|_{C_4} = \left[ \left(\frac{h_\beta}{2}\right) * I_3 \quad 0 * I_3 \quad I_3 \quad \left(\frac{h_{\beta^2}}{4}\right) * I_3 \quad \left(-\frac{l_{\gamma^2}}{8}\right) * I_3 \right]$$

## 2.4 Global Residual Vector

Residual vector can be calculated using following expression:

$$\Delta R^{(\beta\gamma)} = T_1^{(\beta\gamma)} \Delta X^{(\beta\gamma)} + T_2^{(\beta_1\gamma)} \Delta X^{(\beta_1\gamma)} + T_3^{(\beta\gamma_1)} \Delta X^{(\beta\gamma_1)} - D_1^{(\beta\gamma)} \Delta \bar{\epsilon} - D_2^{(\beta_1\gamma)} \Delta \bar{\epsilon} - D_3^{(\beta\gamma_1)} \Delta \bar{\epsilon} \quad (2.22)$$

Where,

$$\Delta X^{(\beta\gamma)} = \left\{ \Delta W_{(10)}^{(\beta\gamma)}, \Delta W_{(01)}^{(\beta\gamma)}, \Delta W_{(00)}^{(\beta\gamma)}, \Delta W_{(20)}^{(\beta\gamma)}, \Delta W_{(02)}^{(\beta\gamma)} \right\} \quad (2.23)$$

$T_1^{(\beta\gamma)}, T_2^{(\beta_1\gamma)}, T_3^{(\beta\gamma_1)}, D_1^{(\beta\gamma)}, D_2^{(\beta_1\gamma)}$  and  $D_3^{(\beta\gamma_1)}$  can be calculated by using following expressions:

$$T_1^{(\beta\gamma)} = \begin{bmatrix} A_{2(10)} & A_{2(01)} & 0 & -\frac{h_\beta}{2} A_{2(20)} & 0 \\ A_{3(10)} & A_{3(01)} & 0 & 0 & -\frac{l_\gamma}{2} A_{3(02)} \\ 0 & 0 & 0 & A_{2(20)} & A_{3(02)} \\ -\frac{h_\beta}{2} I & 0 & I & \frac{h_\beta^2}{4} I & 0 \\ 0 & \frac{l_\gamma}{2} I & I & 0 & \frac{l_\gamma^2}{4} I \end{bmatrix}$$

$$T_2^{(\beta_1\gamma)} = \begin{bmatrix} -A_{2(10)} & -A_{2(01)} & 0 & -\frac{h_\beta}{2} A_{2(20)} & 0 \\ 0 & 0 & 0 & 0 & 0 \\ 0 & 0 & 0 & 0 & 0 \\ -\frac{h_\beta}{2} I & 0 & -I & -\frac{h_\beta^2}{4} I & 0 \\ 0 & 0 & 0 & 0 & 0 \end{bmatrix}$$

$$T_3^{(\beta\gamma_1)} = \begin{bmatrix} 0 & 0 & 0 & 0 & 0 \\ -A_{3(10)} & -A_{3(01)} & 0 & 0 & \frac{l_{\gamma_1}}{2} A_{3(02)} \\ 0 & 0 & 0 & 0 & 0 \\ 0 & 0 & 0 & 0 & 0 \\ 0 & \frac{l_{\gamma_1}}{2} I & -I & 0 & \frac{l_{\gamma_1}^2}{4} I \end{bmatrix}$$



$$D_1^{(\beta\gamma)} = \begin{bmatrix} -A_{2(00)} \\ -A_{3(00)} \\ 0 \\ 0 \\ 0 \end{bmatrix}, D_2^{(\beta_1\gamma)} = \begin{bmatrix} A_{2(00)} \\ 0 \\ 0 \\ 0 \\ 0 \end{bmatrix} \text{ and } D_3^{(\beta\gamma_1)} = \begin{bmatrix} 0 \\ A_{3(00)} \\ 0 \\ 0 \\ 0 \end{bmatrix}$$

The final system of tangential governing equations is obtained by assembling the contributions made by all the sub-cells  $(N_\beta, N_\gamma)$ . The global  $T_G$  and  $D_G$  matrices are obtained by assembling T and D matrices for all the sub-cells as shown in the Figure 2.4.

$$\Delta X = \left\{ \Delta X^{(11)}, \Delta X^{(12)}, \Delta X^{(13)}, \Delta X^{(14)}, \dots, \Delta X^{(N_\beta N_\gamma)} \right\} \quad (2.24)$$

Figure 2.4: Global system of equations

Therefore, by solving the following expression displacement micro-variables can be estimated.

$$S = T_G^{-1} (D_G) \quad (2.25)$$

$$\Delta W = S \Delta \bar{\epsilon} \quad (2.26)$$

The overall tangential stiffness matrix for RUC is calculated using the following expression:

$$C_{eff} = \frac{1}{HL} \sum_{\beta=1}^{N_\beta} \sum_{\gamma=1}^{N_\gamma} h_\beta l_\gamma C^{(\beta\gamma)} S^{(\beta\gamma)} \quad (2.27)$$

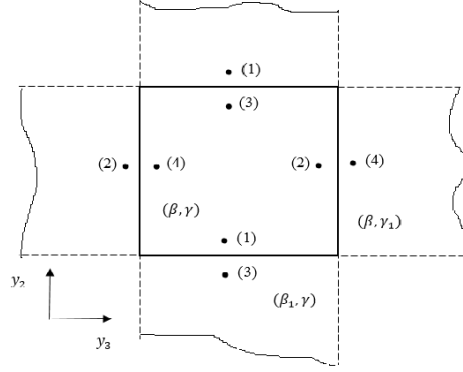


Figure 2.5: Stress integration points on the sub-cell [2]

The residual vector is calculated for every sub-cell by,

$$R^{(\beta\gamma)} = \begin{bmatrix} L_2\sigma^{(\beta\gamma)}_1 - L_2\sigma^{(\beta_1\gamma)}_3 \\ L_3\sigma^{(\beta\gamma)}_2 - L_3\sigma^{(\beta\gamma_1)}_4 \\ L_2\sigma^{(\beta\gamma)}_{(10)} - L_3\sigma^{(\beta\gamma)}_{(01)} \\ 0 \\ 0 \end{bmatrix} \quad (2.28)$$

First two terms in the eq. 2.28 represent traction residual whereas third term represents equilibrium residual. Last two terms in residual vector represent displacement residual which is zero as these equations do not consider stiffness variables. The stresses required to calculate the residual vector are total stresses at stress integration points shown in fig. 2.5 (described in the section A.3)

By assembling residual vectors of each sub-cell, global residual vector is obtained as:

$$R_{Global} = \{R_{(11)}, R_{(12)} \dots R_{(\beta\gamma)} \dots R_{(N_\beta N_\gamma)}\} \quad (2.29)$$

If absolute value of global residual vector is within the tolerance, there is no need to find the correction variables otherwise jacobian matrix is estimated to correct these variables using following expression:

$$\Delta X_{corrected}^i = - \left[ \frac{\partial R_{Global}}{\partial W} \right]_{i-1}^{-1} R_{Global}^i \quad (2.30)$$

where,  $i$  denotes the number of iteration and  $J$  is a jacobian matrix given by following expression:

$$J = - \left[ \frac{\partial R_{Global}}{\partial W} \right]^{-1} \quad (2.31)$$

Displacement micro-variables ( $\Delta W$ ) are calculated using the corrected ( $\Delta X_{corrected}$ ) vector.

## 2.5 Newton - Raphson Iteration Scheme

Newton- Raphson iteration scheme has been used to obtain the solution within error limit. The Figure 2.6 describes steps in the Newton-Raphson iteration scheme. A number of load steps are used to apply the strain in small incremental steps. In this method, it is required to recall the solution of previous iteration or load-step in which assumed solution is to be added. If it is the first iteration of a load step then converged solution of previous load step is added otherwise solution of current iteration is considered.

After estimating the modified micro-variables, strain and stress components are calculated using the solution obtained from previous load step. The local residual vector is calculated for each sub-cell using its corresponding stress variables and by assembling local residual vectors of all the sub-cells, the global residual vector is constructed. If the norm of a global residual vector is within the limit of convergence given by the user then those micro-variables are finalized. Otherwise, the jacobian matrix is given by Eq. 2.31 is calculated which is used for updating the micro-variables and again the same procedure is repeated for next iteration as shown in the Figure 2.6.

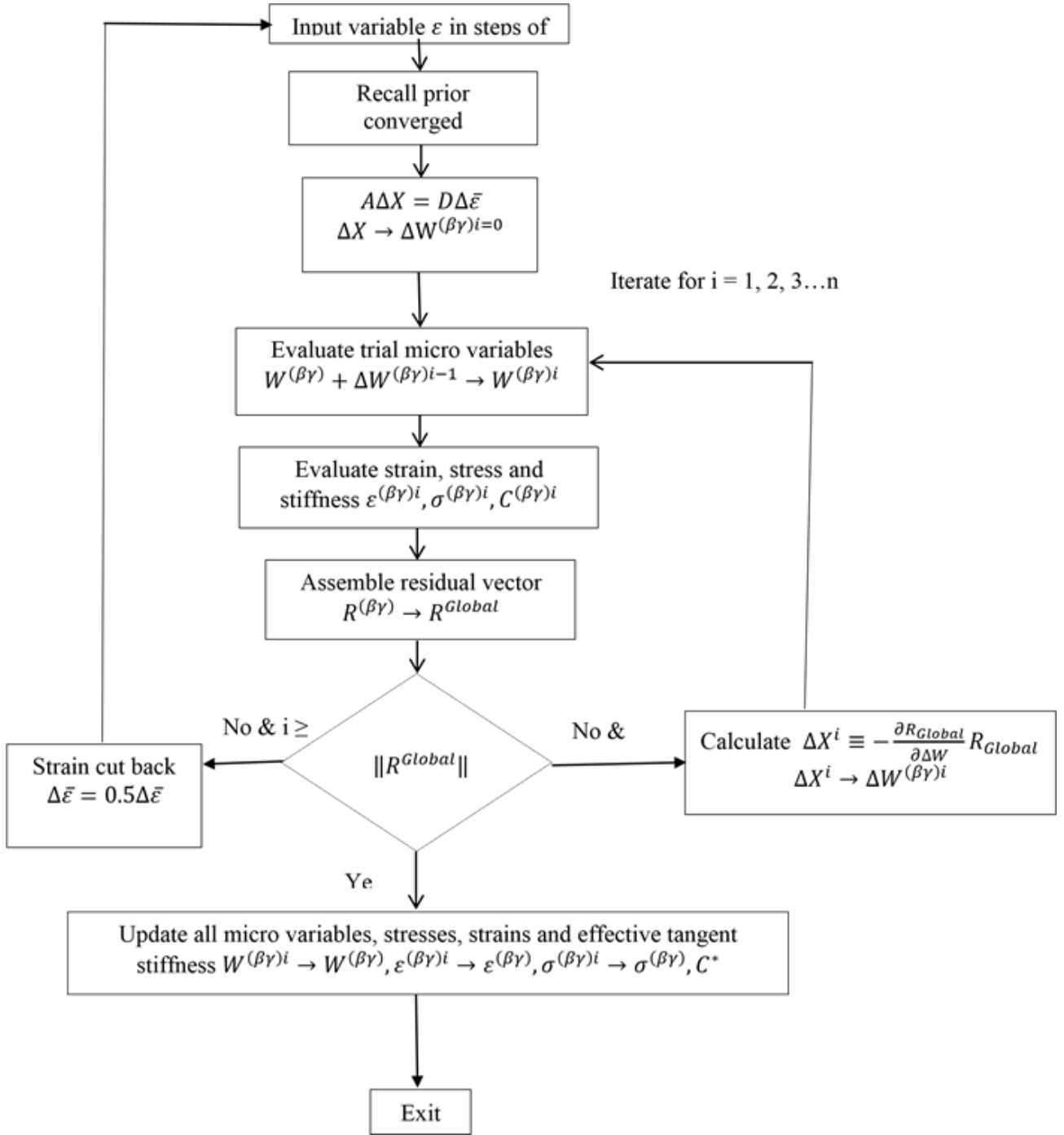


Figure 2.6: Newton Raphson iteration method [3]

## 2.6 Summary

High fidelity generalized method of cells has been discussed in this chapter which is used to calculate the stress and strain variables in the model. Newton-Raphson iteration scheme has been discussed in this chapter to check the convergence at the time of solving global system of equations shown in the Figure 2.4.

## Chapter 3

# Progressive Damage Modeling of Composites

### 3.1 Introduction to PDM

Progressive damage modeling (PDM) is widely employed to study the constitutive behavior of CFRP composite laminate with damage. It allows a detailed study of failure from damage initiation to the final catastrophic failure. It is generally defined in three steps [24, 25, 26, 31, 32, 33] as described below:

1. Stress analysis
2. Damage detection
3. Damage modeling

In the present work, PDM is studied for static loading case. Figure 3.1 describes the steps involved in progressive damage analysis of composite materials. For stress analysis of CFRP model, high fidelity generalized method of cells (HFGMC) has been used which is described in the chapter 2. The second step in the PDM is a damage detection. There are different failure criteria which can be used for damage detection. Amongst which, MCT is used for detecting the damage in the CFRP model. The choice of selection for this failure criteria is in its convenience to provide unified damage index. The different failure modes observed in composites like fiber failure due to tensile or compressive loading, matrix failure due to tensile or compressive loading, shear failure can be captured using multi-continuum theory [37]. Once the damage is detected, properties of the failed elements are to be degraded using certain material property degradation rule. There are mainly two material property degradation rules mentioned in literature review, sudden degradation and continuous degradation

[24, 25, 26, 31]. Here, sudden material property degradation rule is used for damage modeling of composites.

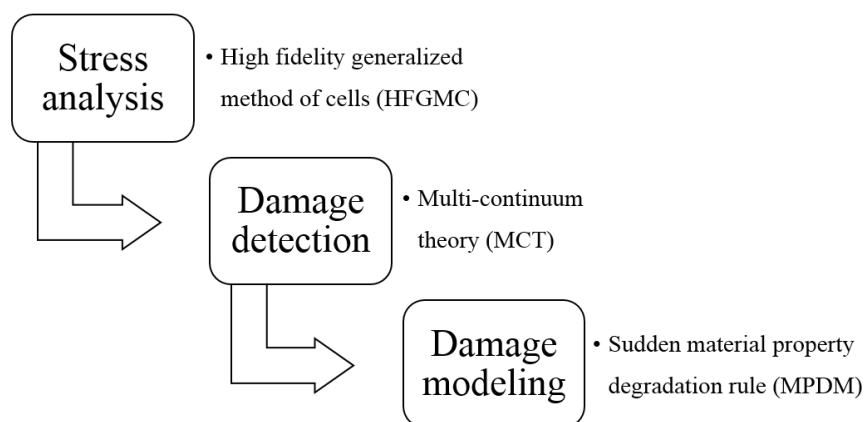


Figure 3.1: Steps in progressive damage modeling

## 3.2 Damage Detection

In progressive damage modeling, second step is to predict the damage in composite material. There are different failure criteria which can be used for damage detection such as:

1. Maximum stress criterion [4, 38]
2. Maximum strain criterion [4, 35]
3. Tsai-Wu-Hill criterion [39]
4. Hashin's failure criterion [26, 33]
5. Multi-continuum theory [36, 37]
6. LARC 03 criterion [35]

These failure criteria can be broadly divided into two groups, failure criterion which include interactions and criterion which neglect the interaction effect due to different stress components. Maximum stress and maximum strain criterion does not consider the effect due to interaction between different stress components. While, Tsai-Wu, Hoffmann, Hashin, LARC 03 and MCT consider the effect of interaction of stress components [35]. Further, these criteria are divided into two groups:

- Criteria which consider single inequality to define the fracture index

- Criteria which consider a combination of interactive and non-interactive conditions for calculating the fracture index

The Hoffman and Tsai-Wu are quadratic criteria and they belong to the first group. While, Hashin, MCT and LARC 03 criteria belong to second group [35]. Among the above-mentioned criteria, we have focused on MCT.

### 3.2.1 Multi-continuum theory

In this theory, it is assumed that fibers are linear elastic in nature and matrix material exhibits nonlinear elastic behavior. It is assumed that fiber and matrix material are perfectly bonded. This is a constituent based failure criterion used to construct a nonlinear progressive failure algorithm for investigating the material failure strengths of composite laminates. MCT is mainly developed for linear elastic and viscoelastic materials. The homogenized value used to characterize the stress tensor at a point in a single continuum material is obtained by taking a volume average of all stresses in the specified region. Composite material is made up of two constituents, fiber and matrix. Stress values for those two materials over specified region are as follows [36, 37, 40]:

$$\begin{aligned}\sigma_f &= \frac{1}{V_f} \int_{D_f} \sigma_x dV \\ \sigma_m &= \frac{1}{V_m} \int_{D_m} \sigma_x dV\end{aligned}\quad (3.1)$$

Where,  $V_f$  and  $V_m$  are the volume fraction of fiber and matrix respectively.

Now, stress ( $\sigma$ ) and strain ( $\epsilon$ ) in the composite material are as follows:

$$\begin{aligned}\sigma &= \sigma_f \phi_f + \sigma_m \phi_m \\ \epsilon &= \epsilon_f \phi_f + \epsilon_m \phi_m\end{aligned}\quad (3.2)$$

Where,  $\phi_f$  and  $\phi_m$  are the volume fractions of fiber and matrix respectively.

The stress and strain components in the fiber and matrix material are defined below:

	Stress	Strain
Fiber	$\sigma_f = C_f \epsilon_f$	$\epsilon_f = \frac{1}{\phi_f} (\epsilon - \epsilon_m \phi_m)$
Matrix	$\sigma_m = C_m \epsilon_m$	$\epsilon_m = (\phi_m [I] + \phi_f [A])^{-1} \left( \frac{\sigma}{C} \right)$



Where,

$$[A] = -\frac{\phi_m}{\phi_f} ([C] - [C_f])^{-1} ([C] - [C_m]) \quad (3.3)$$

Where,  $C_f$  and  $C_m$  are the stiffness matrix of the fiber and matrix material respectively.

Using the obtained strain components, we can calculate strength variables for matrix and fiber material as follows:

Matrix material	
$s_{22}^{mt}$	Matrix transverse tensile strength
$s_{22}^{mc}$	Matrix transverse compressive strength
$s_{12}^{ms}$	Matrix in-plane shear strength
Fiber material	
$S_{11}^{ft}$	Fiber longitudinal tensile strength
$S_{11}^{fc}$	Fiber longitudinal compressive strength
$S_{12}^{fs}$	Fiber in-plane shear strength

For transversely isotropic material, the five stress invariants are as follows:

$$\begin{aligned} I_1 &= \sigma_{11} \\ I_2 &= \sigma_{22} + \sigma_{33} \\ I_3 &= \sigma_{22}^2 + \sigma_{33}^2 + 2\sigma_{23}^2 \\ I_4 &= \sigma_{12}^2 + \sigma_{13}^2 \\ I_5 &= \sigma_{22}\sigma_{12}^2 + \sigma_{33}\sigma_{13}^2 + 2\sigma_{12}\sigma_{13}\sigma_{23} \end{aligned}$$

The general form for a stress interactive failure criterion,

$$K_1 I_1^2 + K_2 I_2^2 + K_3 I_3 + K_4 I_4 = 1 \quad (3.4)$$

Where, the constants  $K_1$ ,  $K_2$ ,  $K_3$  and  $K_4$  are calculated using following expressions:

	$K_1$	$K_2$	$K_3$	$K_4$
Fiber tension	$\frac{1}{S_{11ft}^2}$	-	-	$\frac{1}{S_{12fs}^2}$
Fiber compression	$\frac{1}{S_{11fc}^2}$	-	-	$\frac{1}{S_{12fs}^2}$
Matrix tension	-	$\frac{1}{(S_{22mt}+S_{32m})^2} \left(1 - \frac{S_{22mt}^2+S_{33m}^2}{2S_{23m}^2}\right)$	$\frac{0.5}{S_{22mt}^2}$	$\frac{1}{S_{12ms}^2}$
Matrix compression	-	$\frac{1}{(S_{22mc}+S_{32m})^2} \left(1 - \frac{S_{22mc}^2+S_{33m}^2}{2S_{23m}^2}\right)$	$\frac{0.5}{S_{22mc}^2}$	$\frac{1}{S_{12ms}^2}$

Fiber failure criterion is,

When $\sigma_{11} \geq 0$	When $\sigma_{11} < 0$
$K_{1ft}I_{1f}^2 + K_{4ft}I_{4f} = 1$	$K_{1fc}I_{1f}^2 + K_{4fc}I_{4f} = 1$

Matrix failure criterion is,

When $\sigma_{22} + \sigma_{33} \geq 0$	When $\sigma_{22} + \sigma_{33} < 0$
$K_{3mt}I_{3m} + K_{4mt}I_{4m} = 1$	$K_{3mc}I_{3m} + K_{4mc}I_{4m} = 1$

### 3.3 Damage Modeling

Damage modeling explains how to degrade stiffness and strength properties of the failed sub-cells. Sudden degradation rule has been used for damage modeling in this study. In the current problem the load is increased monotonically, and at critical load point, material fails by one or more failure modes. Depending upon the failure mode detected the material is degraded as per the given in the Table 3.1, the corresponding stiffness properties are degraded for relevant failure mode.

#### 3.3.1 Sudden material property degradation rule (MPDM)

Once the failure is detected in any sub-cell, the properties of that sub-cell is degraded. That is, the failed sub-cell is replaced by an identical sub-cell with degraded material properties. There are various degradation rules available in literature [25, 32] like sudden degradation, continuous degradation, etc.

The degradation rule proposed by Tserpes et.al. [31] is used in this study which is summarized in the Table 3.1 below:

Table 3.1: Degradation rules for various modes of failure

Failure mode	$E_{11}$	$E_{22}$	$E_{33}$	$G_{12}$	$G_{23}$	$G_{13}$	$\nu_{12}$	$\nu_{23}$	$\nu_{13}$
Tensile fiber failure	X			X		X	X		X
Compressive fiber failure	X			X	X	X	X		X
Tensile matrix failure		X	X		X			X	
Compressive matrix failure		X	X		X			X	
More than 1 failure	X	X	X	X	X	X	X	X	X

When the tensile or compressive fiber failure takes place, sub-cell fails to take the load in the fiber direction as the fiber is the main load carrying member in that direction. Thus all the properties in that direction must be degraded. While when matrix cracks are generated along the fiber direction. Thus the material loses load carrying capacity in 2 and 3 direction but all the properties in 1 direction are retained.

### 3.4 Summary

The progressive damage modeling has been explained to study the behavior of CFRP composites. Multi-continuum theory given by Steven [36] has been described to detect the damage in CFRP laminate. Once damage is detected, damage modeling is essential. Therefore, sudden material property degradation rule has been presented for damage modeling.

## Chapter 4

# Prediction of Failure and Stress-strain Behavior of CFRP Laminate

### 4.1 Input Parameters Required for PDM of CFRP Laminate

Carbon fiber reinforced polymer (CFRP) composites are made up of carbon fiber and epoxy resin material. It is assumed that carbon fiber and epoxy resin matrix material are isotropic and homogeneous in nature. Generally, a diameter of the carbon fiber varies between 5-10 micrometer as described by Satish et.al. [6]. Therefore, the average value which is  $7.5 \mu m$  is chosen for further analysis. The matrix material i.e. epoxy resin is prepared from a mixture of LY-556 epoxy resin and HY-951 hardener by Kashfuddoja [5]. The material properties of carbon fiber and epoxy resin which are given in Table 4.1 are obtained experimentally [5] using the digital image correlation (DIC) technique. Further, the dimensions of the RUC configuration are calculated using the properties given in Table 4.1.

Table 4.1: Properties of fiber and matrix material [5]

Material property	carbon fiber	epoxy resin
Shear modulus	88461 MPa	1477 MPa
Poisson's ratio	0.35	0.34
Volume fraction	0.35	0.65

Volume fraction of fiber ( $V_f$ ) can be calculated by using the following expression,

$$V_f = \frac{\left(\frac{\pi}{4}\right) D^2}{L \times H} \quad (4.1)$$

Here, it is assumed that cross section of carbon fiber is circular and RUC is a square. Therefore,

$D$  is the diameter of fiber,  $L$  and  $H$  are the width and height of the RUC respectively as shown in the Figure 2.2a.

By substituting the values in Eq. 4.1 and assuming a square RUC, we obtained  $L = H = 11.235mm$

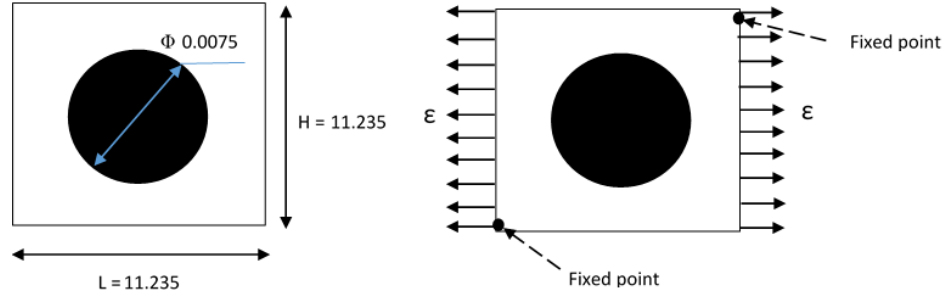


Figure 4.1: RUC Dimension and loading condition (*all the dimensions are in mm*)

RUC is fixed at the two points as shown in the Figure 4.1 and divided as shown in Figure 2.2a into 2500 number of sub-cells. The applied strain is increased from 0 to  $3.715 \times 10^{-3}$ . Using the Eq. 2.27 given by HFGMC method, effective stiffness matrix for RUC is obtained. Further, the material properties of the CFRP composites are calculated using the effective stiffness matrix obtained and compared with the material properties of the CFRP composites calculated using experimental and analytical approach.

## 4.2 Numerical Implementation

The Figure 4.2 describes the steps in progressive damage analysis CFRP laminates. The input parameters required for PDM analysis of CFRP composites are applied strain ( $\epsilon$ ), dimensions of RVE, constituent properties and the number of sub-cells in  $y_2$  and  $y_3$  direction. In the step of material discretization, sub-cells are divided into two groups, fiber and matrix sub-cells based on the distance of sub-cell center from the fiber center. The coordinate system defined for the micromechanical model is a material coordinate system for a composite material.  $x_1$  denotes the fiber direction,  $x_2$  is used for defining ply plane and  $x_3$  describes the perpendicular to ply plane. For visualization of results,  $(x_2, x_3)$  plane is used. Further, local stiffness matrix is calculated for each sub-cell depending on a material of that sub-cell. Fiber and matrix material used are assumed as isotropic and homogeneous in nature. In this step, the constitutive matrix is calculated for each sub-cell considering its isotropic nature. Global  $T_G$  and  $D_G$  matrix are formed using local  $T$  and  $D$  matrices which are calculated using  $P$ ,  $L$  and  $A$  matrices derived in the mathematical formulation of HFGMC. Sparse system solver is used for solving

the global system of equations. Benefits of the sparse implementation are finer unit cell discretization as well as significant improvement of computational effectiveness. By solving the global system equations, displacement, strain and stress components are obtained for each sub-cell. Further, if the solution is in convergence limit, MCT is used for finding the damage state of the sub-cell. Newton-Raphson iteration scheme described by Figure 2.6 is used to obtain the solution in convergence limit. Once the damage is detected, material properties of the failed sub-cells are degraded using sudden material property degradation rule. This process is repeated till the final failure of CFRP composite material. Once the global system has been solved, output variables such as homogenized mechanical properties, strain concentration tensors and failure indexes of the micromechanical failure criteria are plotted. During this PDM analysis described by using Figure 4.2, the residual limit given as  $10^{-10}$  and the final failure is considered when one-third of a total number of sub-cells are failed.

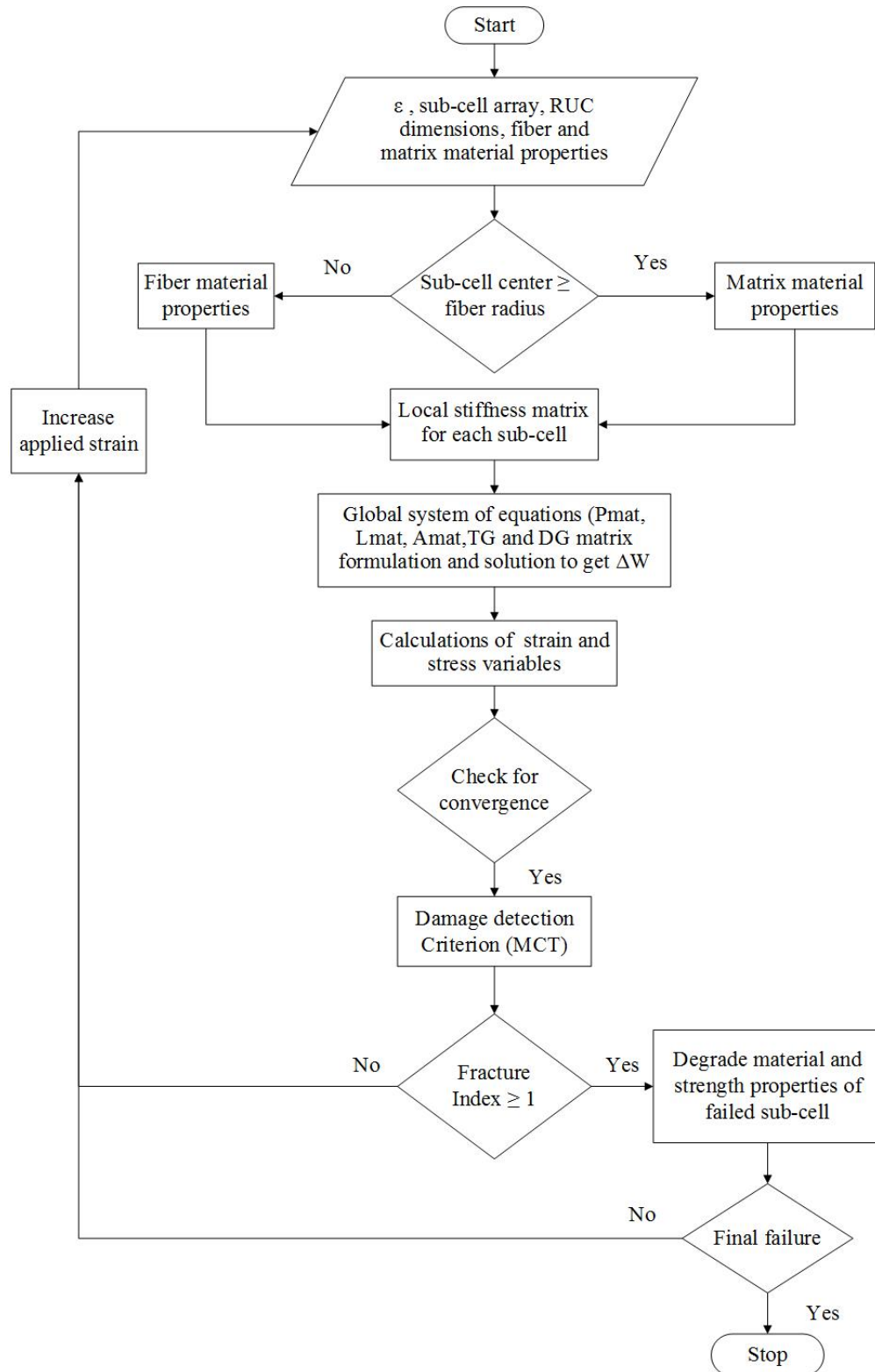


Figure 4.2: Flowchart for HFGMC method [2]

## 4.3 Validation of Numerical Results using Experimental and Analytical Approach

### 4.3.1 Analytical approach

There are two different analytical approaches, rule of mixture and Halpin-Tsai model, which can be used for calculating the material properties of the CFRP composites:

#### 1. Rule of mixture [4, 5]

Rule of a mixture is based on the assumption that property of the composite material is a volume-weighted average of its constituent properties i.e. fiber and matrix. The longitudinal elastic modulus ( $E_1$ ) of CFRP composite can be obtained by using,

$$E_1 = E_f V_f + E_m V_m \quad (4.2)$$

Where,  $E_f$  and  $E_m$  are elastic modulus for fiber and matrix respectively.

The transverse elastic modulus ( $E_2$ ) is obtained by using,

$$E_2 = \frac{E_f E_m}{E_f V_m + E_m V_f} \quad (4.3)$$

The in-plane shear modulus ( $G_{12}$ ) is obtained using,

$$G_{12} = \frac{G_f G_m}{G_f V_m + G_m V_f} \quad (4.4)$$

The in-plane Poisson's ratio ( $\nu_{12}$ ) is obtained using,

$$\nu_{12} = \nu_f V_f + \nu_m V_m \quad (4.5)$$

#### 2. Halpin-Tsai Model [4, 5]

According to Halpin-Tsai semi empirical model, the properties  $E_1$  and  $\nu_{12}$  are same as rule of mixture given by Eq. 4.2 and Eq. 4.5 respectively. The transverse elastic modulus ( $E_2$ ) can be obtained by using,

$$E_2 = E_m \left( \frac{1 + \xi \eta V_f}{1 - \eta V_f} \right) \quad (4.6)$$

$$\eta = \frac{\left( \frac{E_f}{E_m} - 1 \right)}{\left( \frac{E_f}{E_m} + \xi \right)} \quad (4.7)$$

Where,  $\xi = 2$  for circular fiber in square array. It is a reinforcement factor which depends on loading conditions, fiber geometry etc.



The in-plane shear modulus is obtained using,

$$G_{12} = G_m \left( \frac{1 + \xi \eta V_f}{1 - \eta V_f} \right) \quad (4.8)$$

$$\eta = \frac{\left( \frac{G_f}{G_m} - 1 \right)}{\left( \frac{G_f}{G_m} + \xi \right)} \quad (4.9)$$

Where,  $\xi = 1$  for calculating the in-plane shear modulus.

The properties of the carbon fiber and matrix material given in the table 4.1 are used to calculate the properties of CFRP composite laminate analytically by using above mentioned approaches.

Kashddoja [5] has obtained the properties of CFRP composite laminate by performing the DIC experiment. The numerical estimates of material properties are calculated using the effective tensor modulus obtained using Eq. 2.27 by assuming the transversely isotropic nature of composite. The numerically obtained properties are compared with analytically and experimentally obtained results. It can be observed from the Table 4.2 that for  $E_1$ ,  $G_{12}$  and  $\nu_{12}$ , numerical results are closer to experimental results as well as analytical results. There is a percentage error of 2 between the numerical and experimental results for  $E_1$ . However, the numerical and experimental results for  $E_2$  are not comparable. The numerical results for  $E_2$  are closer to the Halpin-Tsai model. The results obtained here are quite consistent with the experimental results obtained by Kashddoja [5].

Table 4.2: Comparison between numerical,experimental and analytical results

Property	HFGMC code results	Experimental results (DIC)	Rule of mixture	Halpin Tsai model
Longitudinal modulus, ( $E_1$ )in GPa	80.25	81.9	83.074	83.074
Transverse modulus, ( $E_2$ )in GPa	8.80	6.15	6.04	9.87
Shear modulus, ( $G_{12}$ )in GPa	2.935	2.77	2.253	2.97
Poisson's ratio, ( $\nu_{12}$ )	0.33	0.34	0.33	0.33

## 4.4 Comparison between Numerical and FEM Results

Initially for preliminary comparison, Stress analysis is carried out by using both high fidelity generalized method of cells and finite element analysis. HFGMC is different from classical finite element method. The major differences are the displacement continuity between adjacent elements is point wise (achieved by node sharing) in the finite elemental method. While in the HFGMC, displacement continuity between adjacent sub-cells is satisfied by an average basis. In HFGMC the equilibrium is

enforced in strong form while the it is enforced in weak form in FEM. In theory, either can be used for stress analysis. However when you introduce gradients the micro-equilibrium handling in weak form is tedious test as compared to HFGMC frame work. Further, in HFGMC, periodic boundary conditions are applied using both displacement and traction continuity whereas in finite element modeling, only displacement continuity is considered.

In the present work, we sought initial comparison of FE simulations without introducing the micro-force balance in the weaker sense. Hence, they cannot be truly compared.

#### 4.4.1 Finite element modeling

A 2D finite element model is developed for CFRP laminate in which SOLID 183 element is used with plane strain condition. Total number of elements used were 54,349 and size of each element was  $5 \times 10^{-5}mm$ . Dimensions and loading condition for RUC are shown in Figure 4.1.

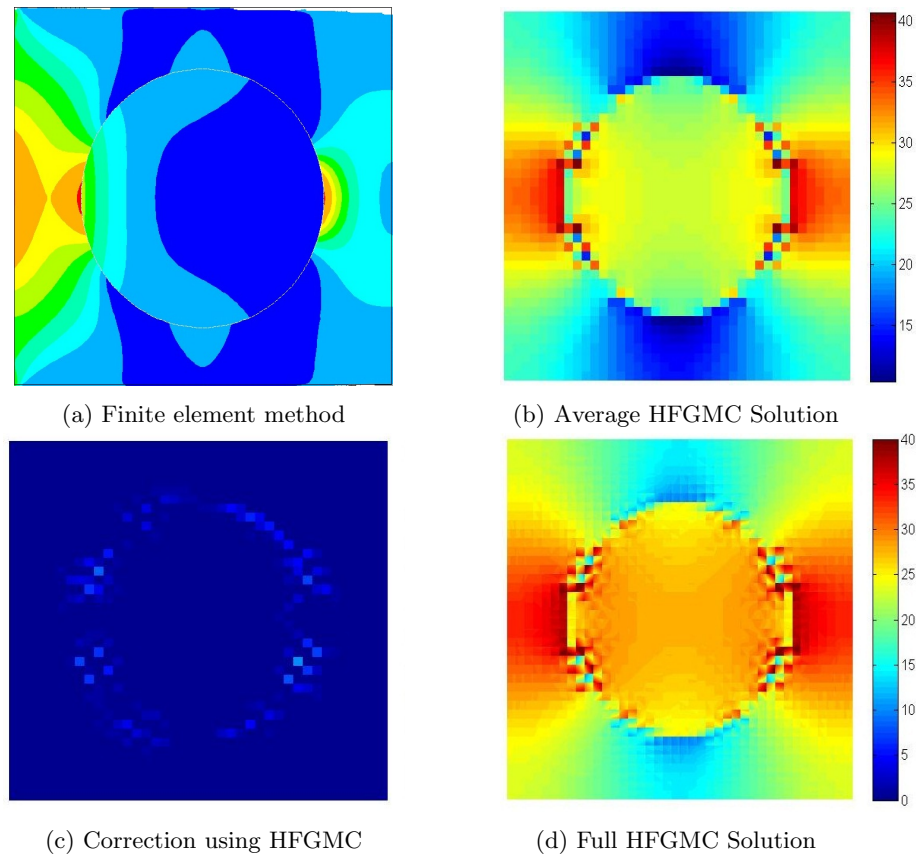


Figure 4.3: Component of stress in fiber direction ( $\sigma_{11}$ )

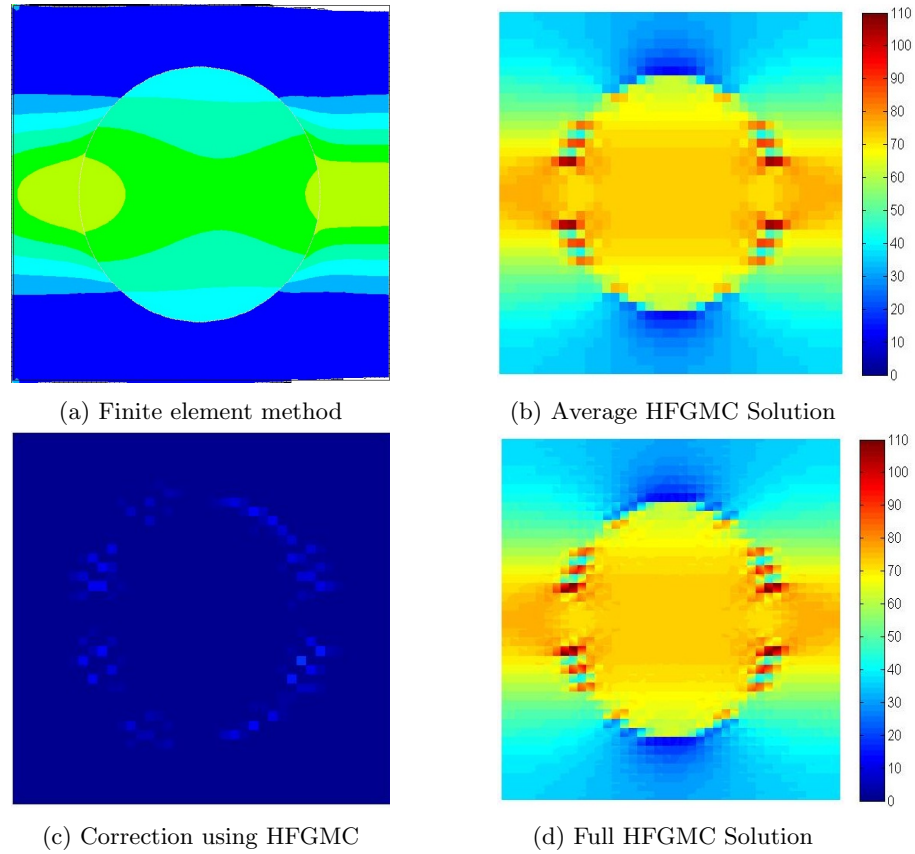


Figure 4.4: Component of stress in loading direction ( $\sigma_{33}$ )

Figures 4.3(a) and (d) shows the stress  $\sigma_{11}$  developed in the fiber direction obtained by finite element method and HFGMC. The HFGMC solution is superposition of average HFGMC solution and the correction due to inhomogeneous field as shown in Figs. 4.3(b) and (c). The FEM and HFGMC agree qualitatively in the pattern. However, HFGMC also provides the inhomogeneous fields due to discrete nature of the inhomogeneity existing at the microscale.

Similarly, Figures 4.4(a) and (d) shows the stress  $\sigma_{11}$  developed in the transverse direction obtained by finite element method and HFGMC. The HFGMC solution is superposition of average HFGMC solution and the correction due to inhomogeneous field as shown in Figs. 4.4(b) and (c).

## 4.5 Stress-strain Behavior of CFRP Composite Laminate

The applied strain has been gradually increased from zero to final failure point and the stress-strain behavior of CFRP composite laminate is reported in here. The dimensions of RUC, loading and boundary conditions are shown in Figure 2.2a. To carry out the analysis, RUC element has been

divided into  $50 \times 50$  sub-cell array.

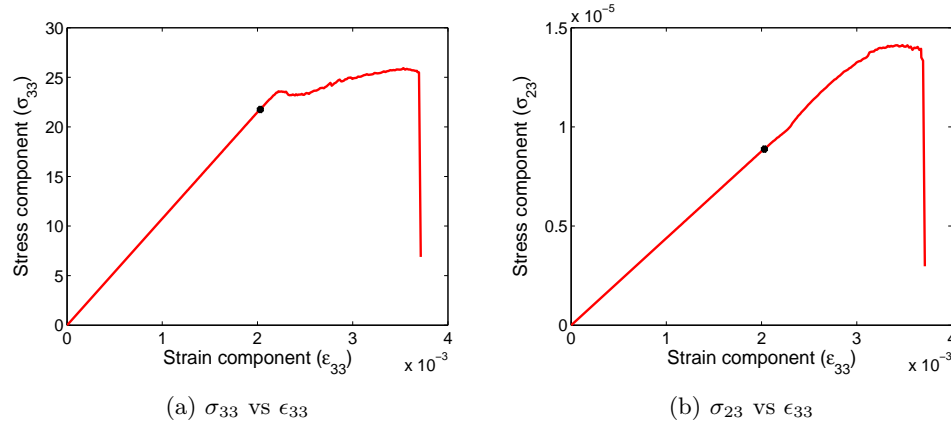


Figure 4.5: Stress-strain curve for CFRP composite

Figures. 4.5a and 4.5b represents the stress ( $\sigma_{33}$  and  $\sigma_{23}$ ) vs applied strain  $\epsilon_{33}$ .

In the figures the black dot represents the damage initiation point at a strain level of  $\epsilon_{33} = 2.03 \times 10^{-3}$ . Simulations are halted and considered as final failure point, when 35 % of total volume is occupied by damaged sub-cells. It can be observed from the figures that, till the damage initiation point, CFRP composite material shows linear behavior but once the damage initiates, softening is observed as shown in Figure 4.5. Softening is due to the sudden degradation in strength (see Bazant [11]). In our simulations, the stiffness properties of the damaged sub-cells were degraded by 95 %. Therefore, strength of the CFRP laminate at damaged location decreases abruptly and softening is observed. Size of the softening region is sensitive to the damaged region. Therefore, to capture the size effect, sub-cell size was varied and the behavior of CFRP composite material following the damage initiation has been observed.

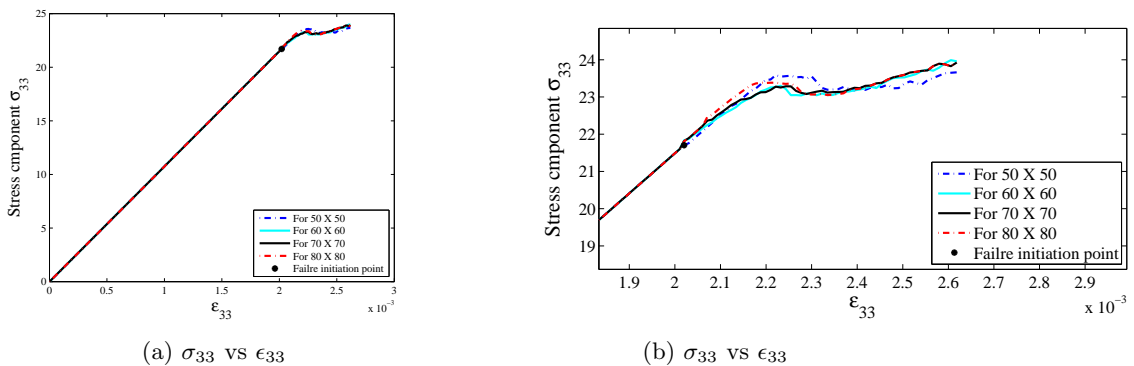


Figure 4.6: Stress-strain curve for different sub-cell array

Figure 4.6a represents the  $\sigma_{33}$  vs  $\epsilon_{33}$  curve for various sub-cell sizes, the stress vs strain linear and damage initiation is converged for the 50x50 and above discretization. However, the zoomed softening zone shown in Figure 4.6b shows that the softening zone is still not converged. But due do limitations in the computing resources,  $50 \times 50$  in the subsequent simulations. The computational cost increases in geometric progression i.e for 70x70 the simulation are 96% more expensive than 50x50 while the predictions are merely improved less than 2%. Further, the softening obtained using sub-cell array of  $50 \times 50$  is more pronounced than others and hence it is on conservative side. Decreasing tendency of softening region could further be seen for finely divided repeating unit cell. However small the subcell size the region of softening always persists [11].

## 4.6 Stress-strain components in the CFRP laminate

The present work is focused on the 2D analysis of CFRP composite laminate. The 2-3 plane is a plane of isotropy. Therefore, stress and strain components with the plane 2-3 are further investigated. In this section, the stress and strain distribution of various components within linear regime (well below damage initiation load) is presented i.e at the applied strain of  $\epsilon = 1.6 \times 10^{-3}$ . Figures 4.7a & 4.7b represents stress  $\sigma_{22}$  and strain  $\epsilon_{22}$  contours for the loaded RUC. Maximum stress has been observed at the transverse hole edge and the corners. The corner nodes are constrained to represent periodic boundary conditions. Hence, reflections are seen from the constrained corner nodes. The stress  $\sigma_{22}$  is non trivial even though pure uniaxial  $\epsilon_{33}$  is applied. The observed stress  $\sigma_{22}$  is purely due to Poisson's effect.

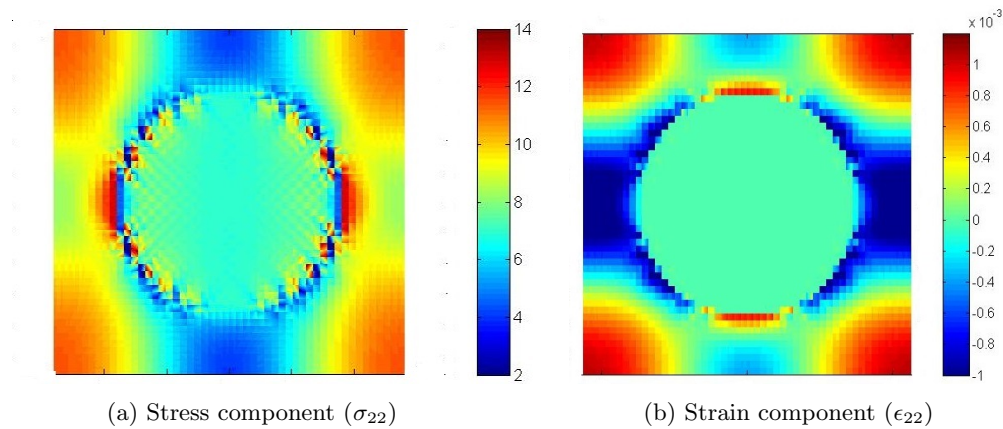


Figure 4.7: Stress and strain component in  $y_2$  direction

Figures 4.8a & 4.8b represents stress  $\sigma_{33}$  and strain  $\epsilon_{33}$  contours for the loaded RUC. Maximum stress has been observed at an angular offset to the transverse hole edge. The strain contours show

low strains in the fiber due to higher stiffness (stiffness ratio is of the order of 60 in this case).

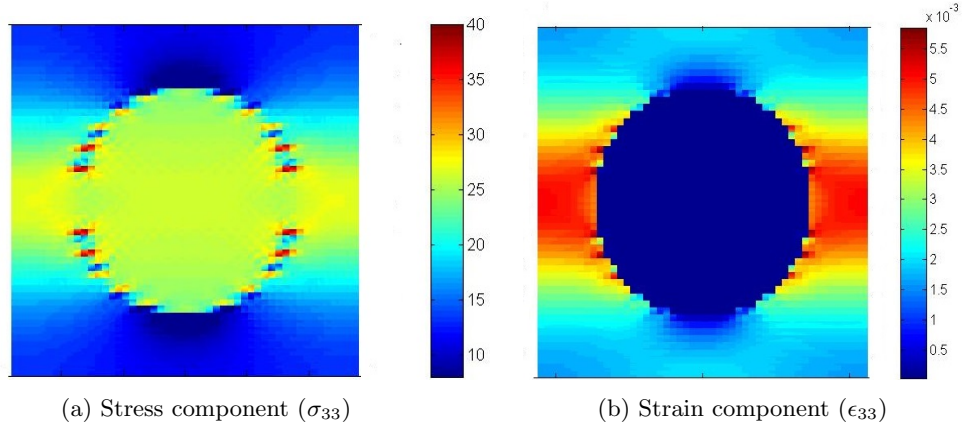


Figure 4.8: Stress and strain component in  $y_3$  direction

Figures 4.9a and 4.9b represent shear stress  $\sigma_{23}$  and shear strain  $\epsilon_{23}$  contours for the loaded RUC. Maximum and minimum stress are observed at  $\pm 45^\circ$  to the transverse hole edge. The inhomogeneous field around the circumference of the hole is greatly spread as compared to normal and transverse field plotted in Figures 4.7a and 4.8a.

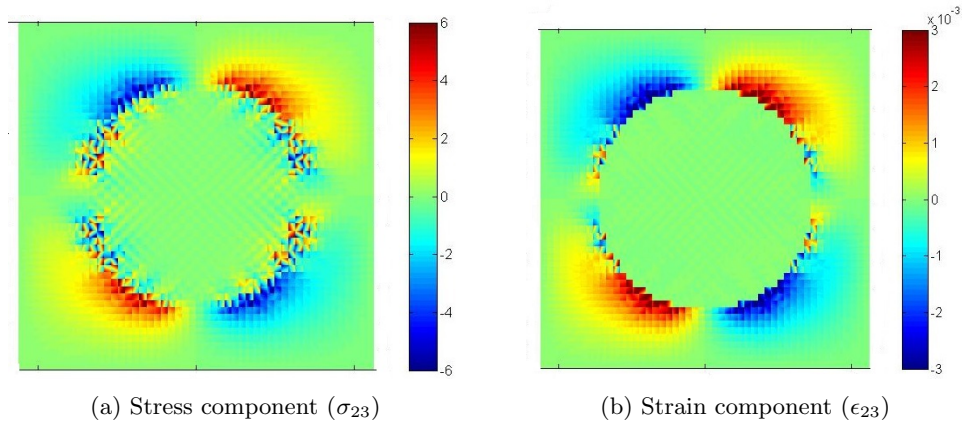


Figure 4.9: Stress and strain component in 2-3 direction

## 4.7 Damage Propagation in CFRP Laminate

To study the damage behavior of CFRP composites, applied strain is increased from 0 to the final failure point. The Figure 4.11 shows the variation of volume fraction of damage with increasing strain value. Till  $\epsilon = 2.21 \times 10^{-3}$ , damage was absent but after increasing the strain further, non-linear variation has been observed. The plot of the volume fraction of damage versus strain follows cubic



nature as observed from Figure 4.11 after failure initiation point. The cubic expression obtained by using basic fitting in MATLAB R2013a is as follows:

$$V_{damage} = 4.13 \times 10^7 \epsilon_{33}^3 - 3.58 \times 10^5 \epsilon_{33}^2 + 1219.5 \epsilon_{33} - 1.3634$$

Final failure has been observed when 35 % volume of the material was damaged.

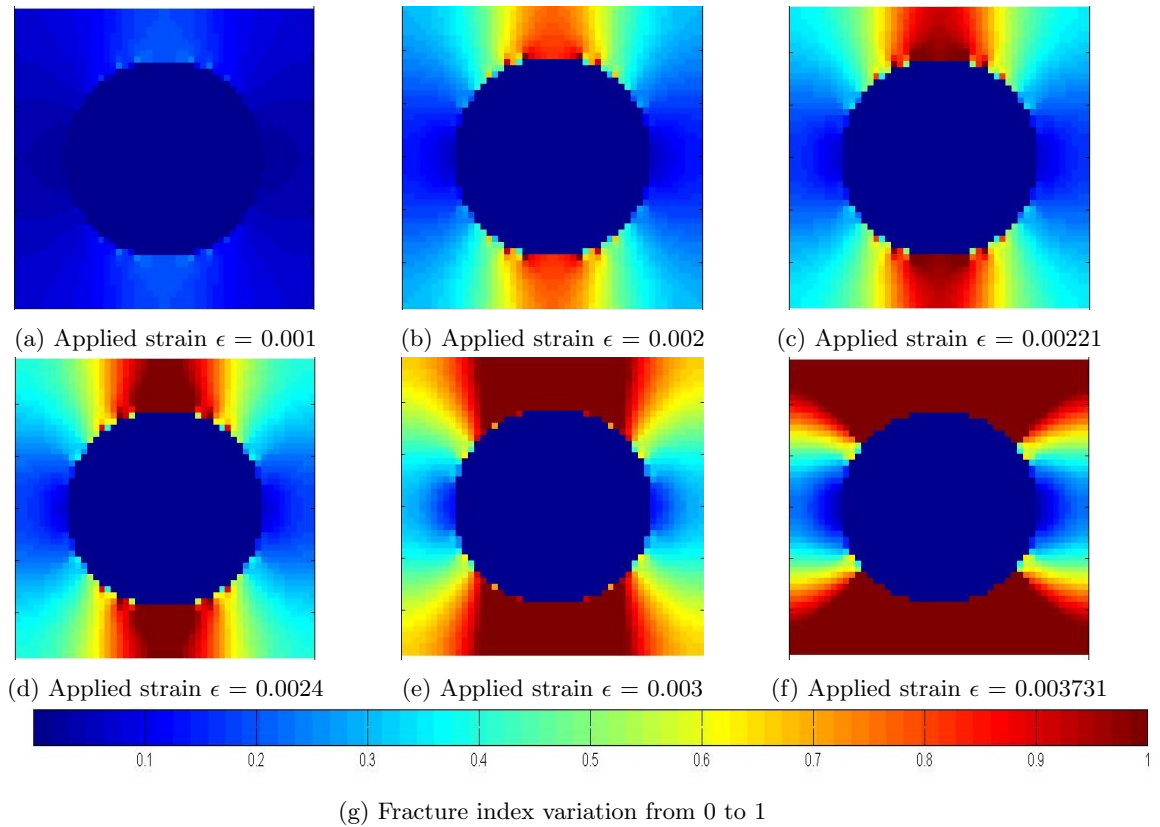


Figure 4.10: Damage propagation in CFRP composite material with increasing strain

Figure 4.10 shows the damage behavior of CFRP composite material. In this figure, fracture index variation for different strain values is plotted for single RUC element. The dimensions of RUC are kept as shown in Figure 4.1. As the fracture index reaches to 1 for any sub-cell of RUC, that sub-cell is assumed to be failed. From Figure 4.10c, it is observed that failure initiates for  $\epsilon = 0.00221$  applied strain value and four sub-cells are failed. From Figure 4.10a and Figure 4.10b, it is observed that there is no failure till the applied strain reaches to  $\epsilon = 0.00221$ .

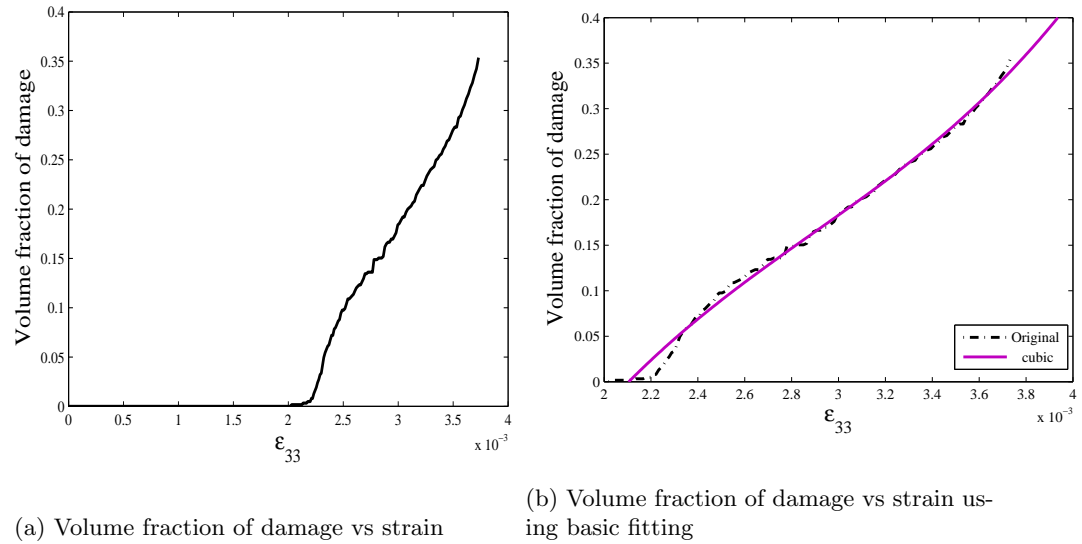


Figure 4.11: Volume fraction of damage with increasing strain

The stiffness and strength properties of the failed sub-cells are degraded by 95 % and again applied strain is increased. Now, as applied strain increases, failure propagates in the direction of loading as shown in Figure 4.10d. For this strain, the failed sub-cells are 124.

Failure propagation is observed for  $\epsilon = 0.003$  as shown in Figure 4.10e. Till this point number of failed sub-cells are 464. Again, same procedure is repeated as mentioned for previous case. Now, catastrophic failure is observed for  $\epsilon = 0.003731$  as shown in Figure 4.10f with 884 failed sub-cells. All failed sub-cells are from matrix region.

## 4.8 Stiffness Properties of CFRP Composite Laminate

The variation of stiffness properties of CFRP laminate with the increasing strain from 0 to  $3.3715 \times 10^{-3}$  is shown in Figure 4.12. Behavior of all the stiffness properties is constant till the damage initiation point ( $\epsilon = 2.02 \times 10^{-3}$ ) however non-consistent beyond that.



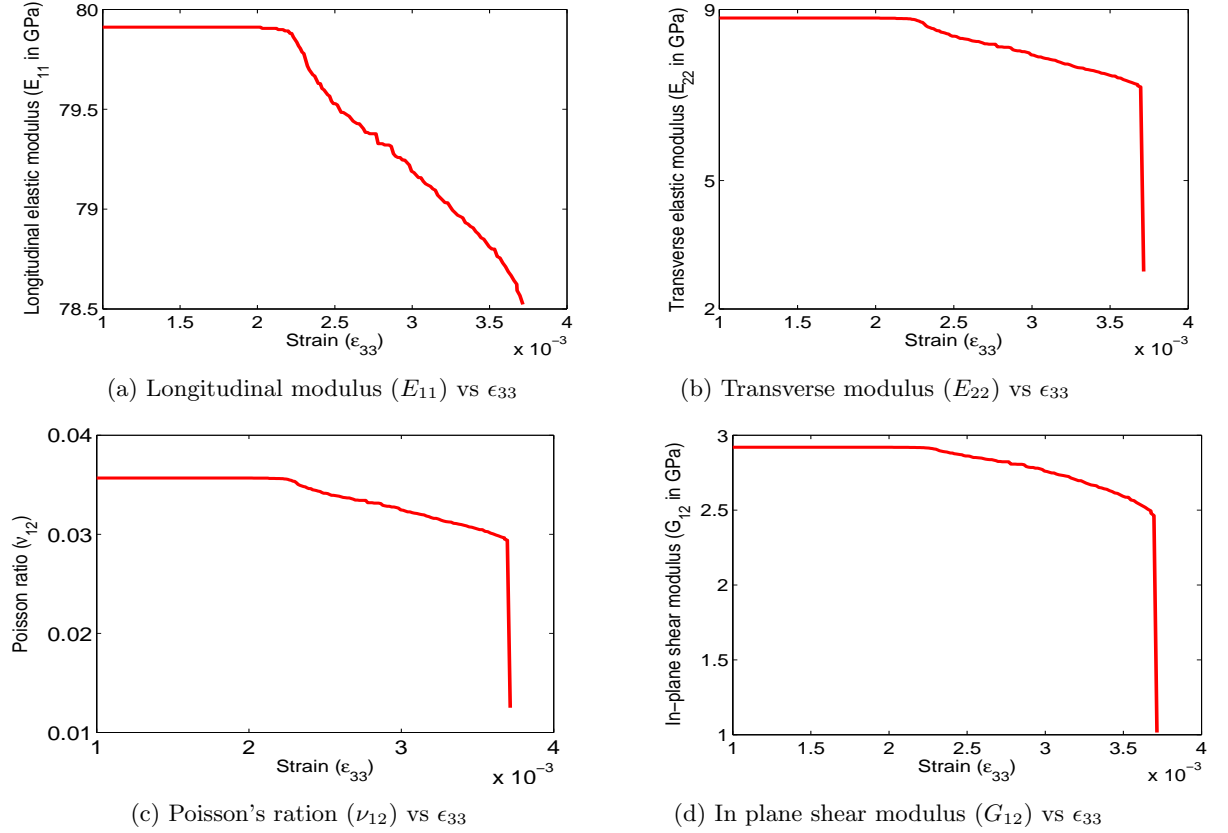
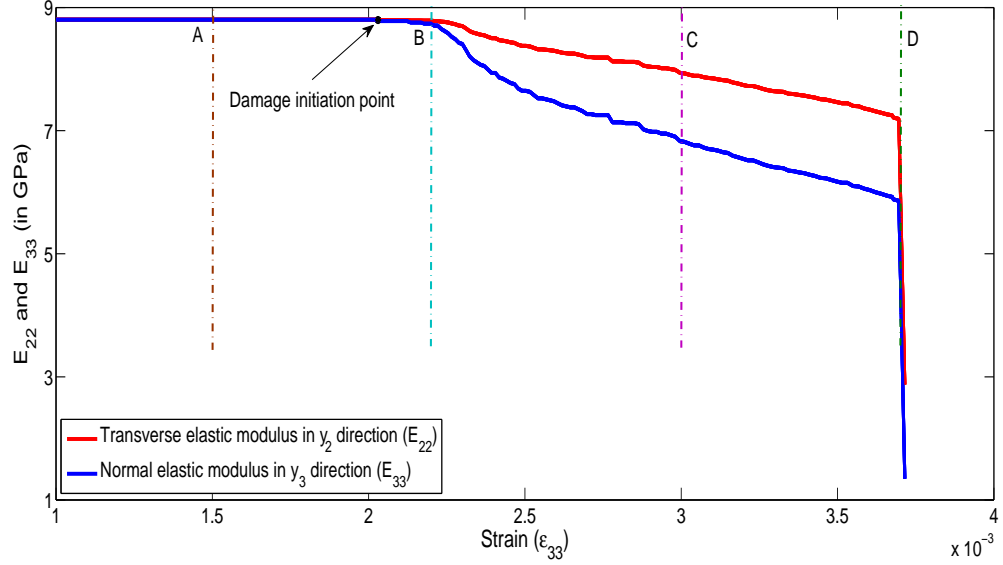


Figure 4.12: Properties of CFRP composite with increasing applied strain

From Figure 4.12, the nature of deterioration of stiffness properties beyond failure initiation point can be observed in which, longitudinal elastic modulus  $E_{11}$  gradually degrades till final failure point ( $\epsilon = 3.71 \times 10^{-3}$ ) whereas others exhibits sudden drop. The Figure 4.13 shows the variation of  $E_{22}$  and  $E_{33}$  properties with increasing strain. It is observed from this figure that  $E_{22}$  and  $E_{33}$  retain same value till failure initiation point beyond which, both the values degrades differently till final failure point. CFRP laminate has only five independent constants in the effective constitutive matrix till failure initiation point. The effective stiffness matrix for the RUC in the linear region before damage initiation ( $C_A^{eff}$ ) is given below:

$$C_A^{eff} = \begin{bmatrix} 83100 & 4921 & 4921 & 0 & 0 & 0 \\ 4921 & 10743 & 4446 & 0 & 0 & 0 \\ 4921 & 4446 & 10743 & 0 & 0 & 0 \\ 0 & 0 & 0 & 2384 & 0 & 0 \\ 0 & 0 & 0 & 0 & 2920 & 0 \\ 0 & 0 & 0 & 0 & 0 & 2920 \end{bmatrix}$$

Figure 4.13: Comparison between  $E_{22}$  and  $E_{33}$  properties

From the above stiffness matrix, it is observed that

$$c_{22} = c_{33}, c_{21} = c_{31}, c_{55} = c_{66}, c_{44} = \frac{1}{2}(c_{22} - c_{23}) \text{ and all other constants are zero.}$$

Therefore, it is clearly seen that  $(y_2, y_3)$  plane shows transversely isotropic behavior till damage initiation point. In this plane, the stiffness properties are constant when calculated in different directions till damage initiation point. Therefore, stiffness matrix at the point where stiffness properties starts degrading which can be called as corporation point which is  $(C_B^{eff})$ ,

$$(C_B^{eff}) = \begin{bmatrix} 83076 & 4912 & 4897 & 0 & 0 & 0 \\ 4909 & 10727 & 4427 & 0 & 0 & 0 \\ 4901 & 4436 & 10691 & 0 & 0 & 0 \\ 0 & 0 & 0 & 2376 & 0 & 0 \\ 0 & 0 & 0 & 0 & 2905 & 0 \\ 0 & 0 & 0 & 0 & 0 & 2918 \end{bmatrix}$$

The effective stiffness matrix at  $\epsilon = 3 \times 10^{-3}$  which is in the region between damage initiation and final failure is given by  $(C_C^{eff})$ ,

$$(C_C^{eff}) = \begin{bmatrix} 81799 & 4332 & 3736 & 0 & 0 & 0 \\ 4220 & 9615 & 3476 & 0 & 0 & 0 \\ 3920 & 3848 & 8239 & 0 & 0 & 0 \\ 0 & 0 & 0 & 2023 & 0 & 0 \\ 0 & 0 & 0 & 0 & 2257 & 0 \\ 0 & 0 & 0 & 0 & 0 & 2753 \end{bmatrix}$$

The The effective stiffness matrix at final failure point is given by  $(C_D^{eff})$ ,

$$(C_D^{eff}) = \begin{bmatrix} 79483 & 1993 & 965 & 0 & 0 & 0 \\ 1599 & 3947 & 1017 & 0 & 0 & 0 \\ 1240 & 1927 & 1845 & 0 & 0 & 0 \\ 0 & 0 & 0 & 708 & 0 & 0 \\ 0 & 0 & 0 & 0 & 415 & 0 \\ 0 & 0 & 0 & 0 & 0 & 1014 \end{bmatrix}$$

Therefore, by observing  $(C_D^{eff})$  sudden drop has been observed in the stiffness properties at the failure point. The behavior of material changes to anisotropic from isotropic, beyond failure initiation point since the nature of stiffness properties does not remain constant in all direction in the 2-3 plane this claim can be visualized graphically also from the figure 4.13

## 4.9 Summary

The input parameters required for progressive damage analysis of composites have been discussed in this chapter. The steps in the numerical analysis using high fidelity generalized method of cells is also included in this chapter with the help of flowchart shown in the Figure 4.2. The behavior of the CFRP laminate and variation of stiffness properties under increasing strain has been studied in this chapter. The numerical results obtained are compared with experimental results generated by Kashfuddoja [5] and analytical results calculated using Halpin-Tsai model. The damage progression in the laminate has been studied described in the Figure 4.10 with increasing strain and final failure of the CFRP laminate has been captured. II RVE configuration has been analyzed for increasing  $(D/H)$  ratio to find the minimum RVE size.

## Chapter 5

# RVE Interaction Effect

For simplicity, the microstructure of the CFRP composite has been assumed as doubly periodic, shown in the Figure 5.1 which is defined in the  $(x_2, x_3)$  co-ordinate system. RUC element is described by Figure 5.2 defined in the  $(y_2, y_3)$  co-ordinate system. Sometimes, RUC does not represent RVE. In such cases, mean-field homogenization is used to obtain the homogeneous properties of the CFRP composites. Due to non-local effects, RVE is size dependent. Therefore, it is essential to consider the RVE interaction effect. Figure 5.1 shows (Blue) RVE with no interaction, (orange) with near neighbor interaction and (green) with next near neighbor interaction. Due to long-range interactions, the size of the RVE changes. In the present analysis, near neighbor interaction effect has been considered while calculating the minimum RVE size and assumed as next near neighbor effect is absent.

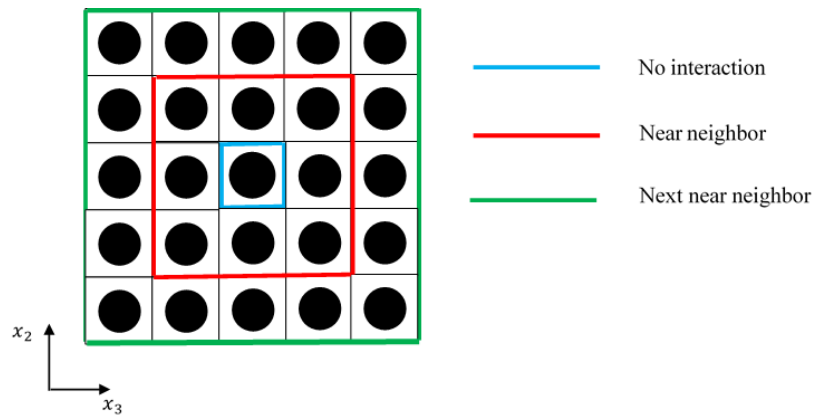


Figure 5.1: Micro-structure of CFRP composite

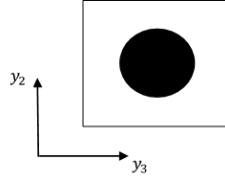


Figure 5.2: Repeating unit cell element in  $(y_2, y_3)$  co-ordinate system

Due to computational limitations, it is prohibitively difficult to solve the global system of equations for the near neighbor interaction RVE shown in the Figure 5.1 with red color. Therefore, to capture the fiber interaction effect, different RVE configurations shown in the Figure 5.3 are considered. This chapter focuses on estimating the minimum RVE size for different RVE configurations shown in the Figure 5.3 for the CFRP composite material using the HFGMC method and Halpin-Tsai model.

1I RVE configuration accounts for a single RUC element as shown in the Figure 5.3 whereas two RUC elements are analyzed in 2IL and 2IT RVE configurations. In 2IT configuration, two fiber elements are placed in the direction perpendicular to the loading and the two fiber elements are deposited in the direction of loading for 2IL RVE configuration as shown in the Figure 5.3.

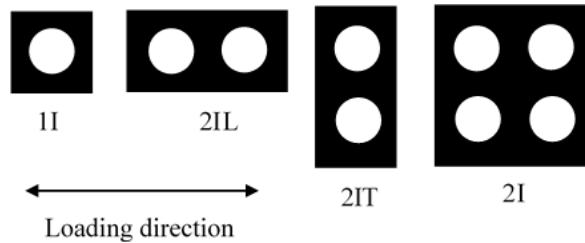


Figure 5.3: Different RVE configurations

2I RVE configuration consists of four RUC elements as shown in the Figure 5.3.

## 5.1 Fiber Interaction Effect

Previously, 1I fiber configuration has been analyzed but the fiber interaction effect present due to the fiber orientation, fiber spacing etc. can not be captured using single fiber RUC element, which is demonstrated by the Figure 5.4.

The fracture index has been plotted for different RVE configurations for same loading condition in the Figure 5.4. As fracture index reaches to 1, the damage is detected in the material. All the RVE configurations described in the Figure 5.3 has been studied for  $\epsilon = 1.6 \times 10^{-3}$  and it is discovered that all other RVE configurations are showing failure except 1I fiber configuration. Therefore, the

necessity of considering different configurations arises. It becomes essential to calculate minimum RVE size for which the fiber interaction effect disappears or shows negligible effect. Therefore, in Chapter 5, different RVE configurations has been studied to find the minimum RVE size.

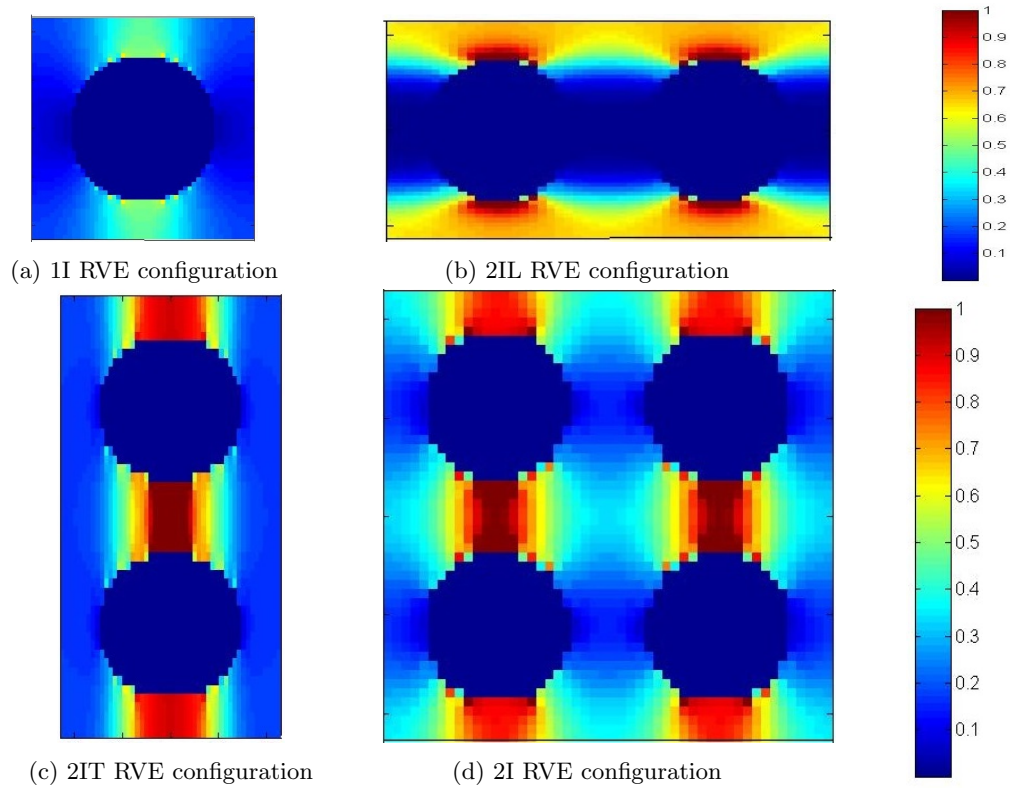
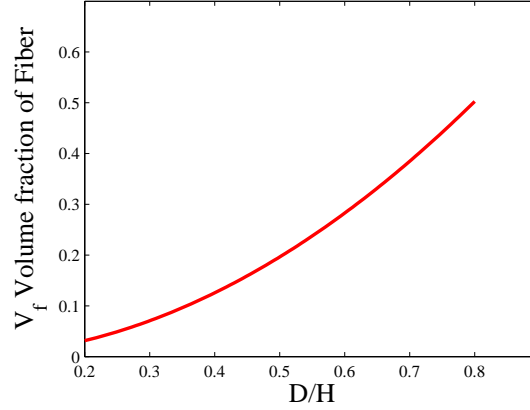


Figure 5.4: Fiber interaction effect in different RVE configurations

## 5.2 Different Types of RVE Configurations

To find the minimum RVE size, RVE configurations has been inspected for the varying ( $D/H$ ) ratio from 0.2 to 0.8 in which,  $D$  and  $H$  are the diameter of the fiber and height of the RVE respectively. In each RVE configuration, diameter of the fiber ( $D$ ) was kept constant which was  $7.5 \mu m$  and the volume fraction of the fiber ( $V_f$ ) was varied between 0.0031 to 0.502 as shown in the Figure 5.5. The dimensions of the RVE configurations has been calculated using the Eq. 4.1 and the properties of the carbon fiber and epoxy resin material has been taken from the Table 4.1.

Figure 5.5: Volume fraction of fiber vs ( $D/H$ )

Dimensions of all the RVE configurations were calculated using the following expression of volume fraction of fiber ( $V_f$ ):

$$V_f = \frac{n \times \left(\frac{\pi}{4}\right) D^2}{L \times H} \quad (5.1)$$

where,  $n$  is the number of fiber elements

$D$  is the diameter of the fiber

$L$  and  $H$  are the width and height of the RVE respectively.

### 5.2.1 1I RVE Configuration:

Single RUC element has been studied in the 1I RVE configuration as shown in the Figure 5.3. The dimensions of the RVE are calculated using the Eq. 5.1. While calculating the dimensions for 1I configuration, it was assumed that  $W = H$ . Using diameter and volume fraction of the fiber shown in the Figure 5.5, dimensions of the 1I RVE are calculated for each ( $D/H$ ) ratio. It can be seen from Figure 5.5, volume fraction of the RVE increases with increase in the ( $D/H$ ) ratio. Dimensions of the RVE, calculated using Eq. 5.1 for different ( $D/H$ ) ratio are given in the Table 5.1. The microstructure of the 1I RVE configuration for mentioned ( $D/H$ ) ratios is shown in the Figure 5.6. The diameter of the fiber element is constant for every ( $D/H$ ) ratio but size of the RVE decreases with increasing ( $D/H$ ) ratio.

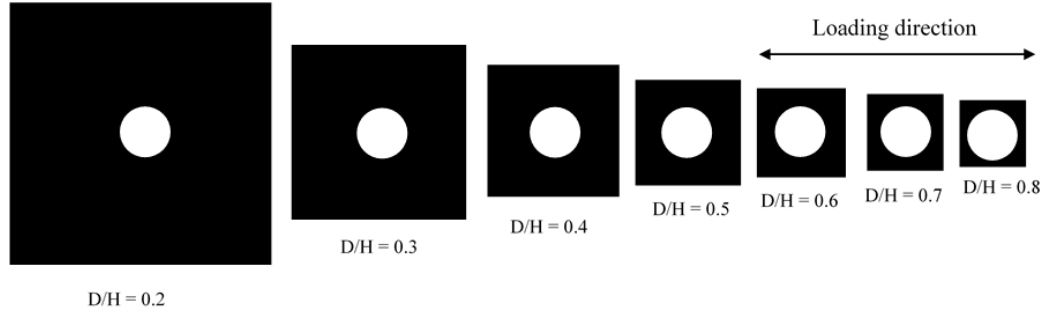


Figure 5.6: Micro-structure for different ( $D/H$ ) ratios for 1I RVE configuration

Table 5.1: Dimensions of 1I RVE configuration for different ( $D/H$ ) ratio  
(all the dimensions are in  $\mu\text{m}$ )

$(D/H)$	Height ( $H$ )	width ( $L$ )	Volume fraction of fiber ( $V_f$ )
0.2	37.5	37.5	0.031
0.3	25	25	0.00706
0.4	18.75	18.75	0.126
0.5	15	15	0.196
0.6	12.5	12.5	0.282
0.7	10.72	10.72	0.384
0.8	9.375	9.375	0.502

Drugan et al. [27, 28] has used Hashin-Shtrikman variational principle to obtain a micro-mechanics based non-local constitutional relation between the stress and strain variables at macro scale. He has calculated the minimum size of RVE by allowing 5% variation in the overall modulus tensor over which the macroscopic properties of the element are constant. In present approach, high fidelity generalized method of cells has been used to find the effective stiffness matrix for the representative volume element and assuming transversely isotropic nature of the CFRP composites, stiffness properties for the 1I RVE configuration of the CFRP composite material has been determined for ( $D/H$ ) ratio varying from 0.2 to 0.8. Halpin-Tsai model described in the section 4.3 is used to calculate the material properties for different ( $D/H$ ) ratios analytically and obtained results are compared with the numerical properties acquired using HFGMC.



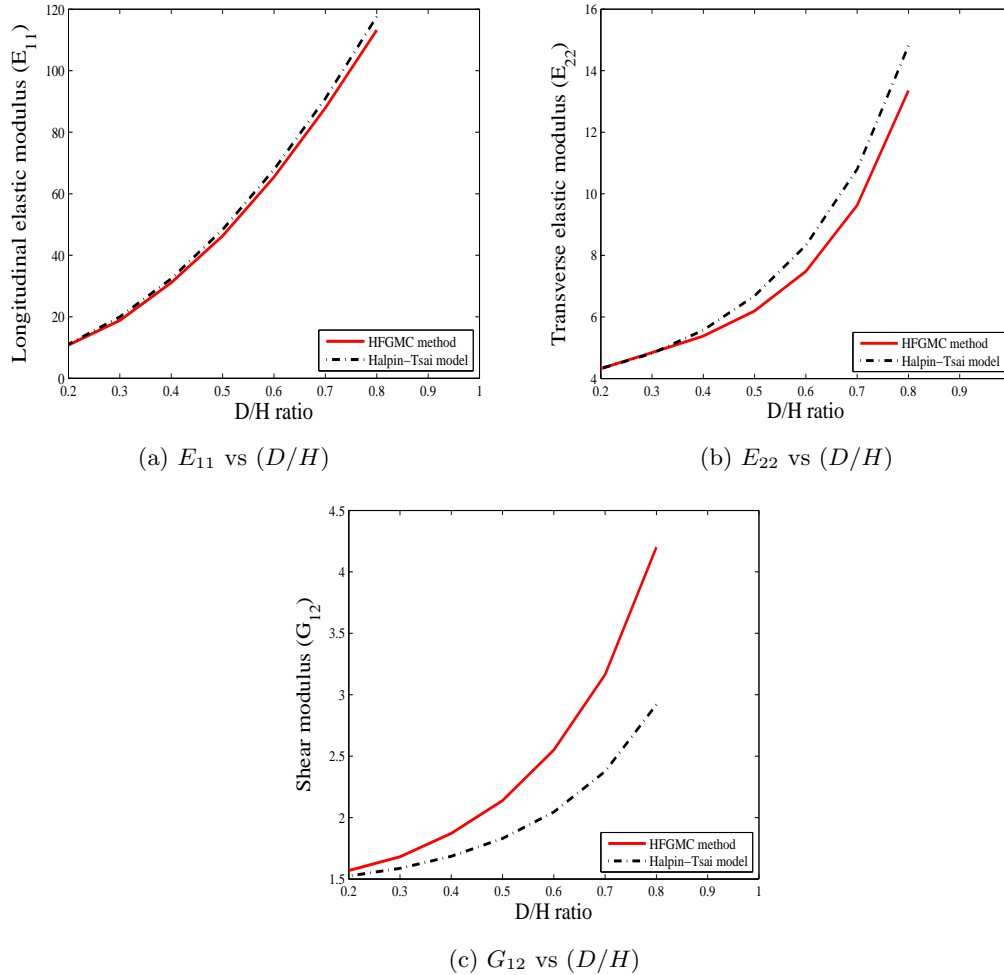


Figure 5.7: Variation in the stiffness properties with increasing  $(D/H)$  ratio for 1I RVE configuration

$E_{11}$ ,  $E_{22}$  and  $G_{12}$  are the longitudinal elastic modulus in the fiber direction, transverse elastic modulus and in-plane shear modulus respectively. The Figure 5.7a presents the difference between the longitudinal elastic modulus ( $E_{11}$ ) obtained using HFGMC method and Halpin-Tsai model for increasing  $(D/H)$  ratio from 0.2 to 0.8. It can be followed from the Figure 5.7a that with decreasing  $(D/H)$  ratio, HFGMC method approaches towards the Halpin-Tsai model. Similar results are observed for transverse elastic modulus ( $E_{22}$ ) and shear modulus ( $E_{22}$ ) illustrated by Figure 5.7b and 5.7c respectively. It can be seen from the Figure 5.7b and 5.7c, error in stiffness properties calculated using HFGMC and Halpin-Tsai method progressively increases with increasing  $(D/H)$  ratio. The particular value of  $(D/H)$  ratio at which above error reaches within the limit of 5 % symbolizes the minimum RVE size. Therefore, for  $(D/H) = 0.4$  or less, all the stiffness properties described in the

Figure 5.7 are within 5% error limit w.r.t analytical results acquired using Halpin-Tsai model. Hence, size of the RVE for  $(D/H) = 0.4$  given in the Table 5.1 is the minimum RVE size for 1I configuration.

### 5.2.2 2IT RVE configuration:

2IT RVE configuration is shown in the Figure 5.3 in which two fiber elements are placed in the direction perpendicular to the loading. Therefore, to capture the fiber interaction effect, 2IT configuration has been studied for various  $(D/H)$  ratios. For 2IT RVE configuration, strain was applied in the length direction as shown in The Figure 5.3.

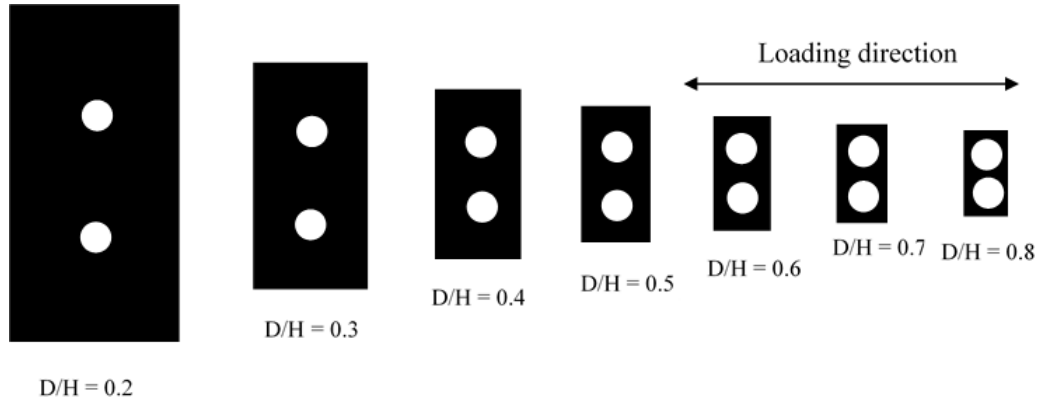


Figure 5.8: Micro-structure for different  $(D/H)$  ratios for 2IT RVE configuration

Dimensions of the RVE has been estimated using the Eq. 5.1 and stated in the Table 5.2. The micro-structure of the 2IT RVE with increasing  $(D/H)$  ratio is presented in the Figure 5.8 in which diameter of both the fiber elements remain constant for all the  $(D/H)$  ratios.

Table 5.2: Dimensions of 2IT RVE configuration for different  $(D/H)$  ratio  
(all the dimensions are in  $\mu m$ )

$(D/H)$	Height ( $H$ )	width ( $L$ )	Distance between center of fibers	Volume fraction ( $V_f$ )
0.2	75	37.5	37.5	0.031
0.3	50	25	25	0.00706
0.4	37.5	18.75	18.75	0.126
0.5	30	15	15	0.196
0.6	25	12.5	12.5	0.282
0.7	21.43	10.72	10.72	0.384
0.8	18.75	9.375	9.375	0.502

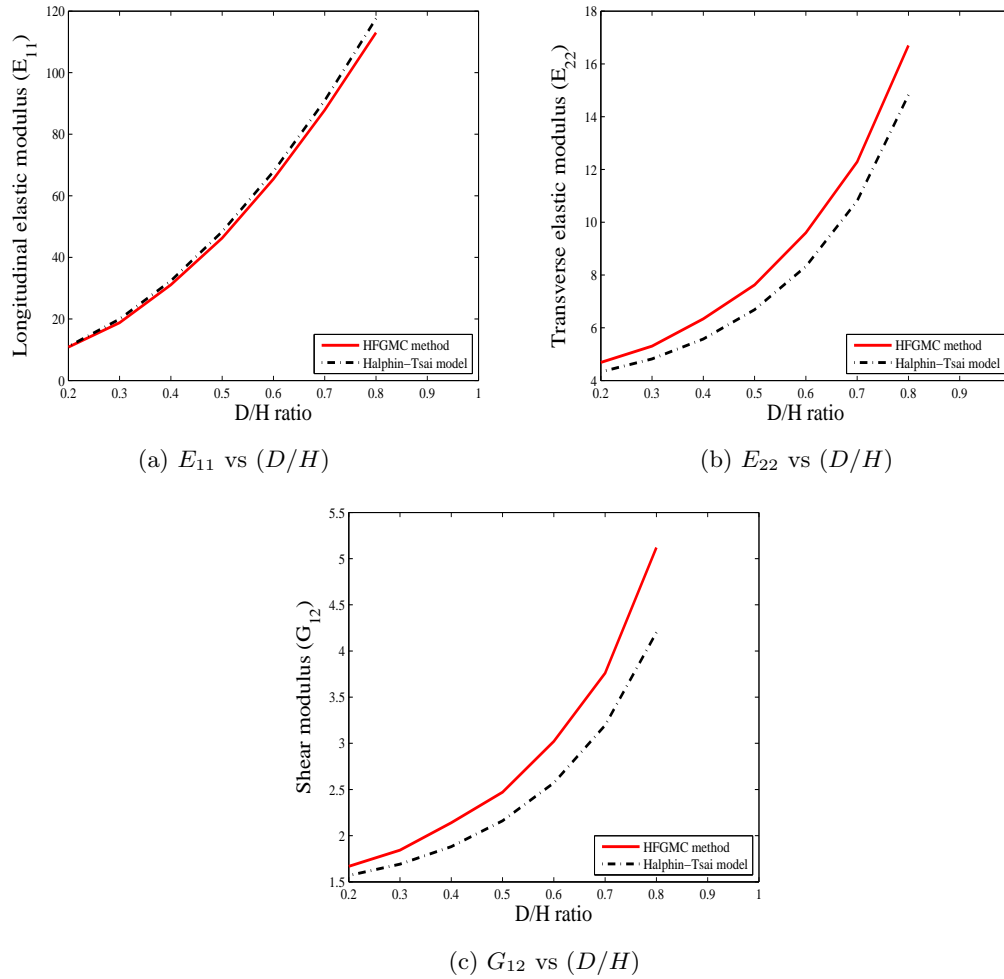


Figure 5.9: Variation in the stiffness properties with increasing  $(D/H)$  ratio for 2IT RVE configuration

The overall modulus tensor for 2IT RVE configuration was obtained using HFGMC method to calculate the stiffness properties of CFRP composite material. Here, the difference between the properties obtained using Halpin-Tsai model and HFGMC method is more when compared with the 1I RVE configuration. It was observed that the percentage change in the stiffness properties calculated using HFGMC method, prescribed in the Figure 5.9 is within 5 % when compared with Halpin-Tsai model for  $(D/H) = 0.3$  and less for 2IT configuration. Therefore, estimated minimum RVE size for 2IT RVE configuration is for  $(D/H) = 0.3$  which is stated in the Table 5.2.

### 5.2.3 2IL RVE configuration

2IL RVE configuration is shown in the Figure 5.3 in which two fiber elements are positioned in the direction of loading. Therefore, to study the behavior of the RVE configuration, strain  $\epsilon = 1 \times 10^{-3}$  has been applied in the direction of fiber and effective stiffness matrix was calculated to find the stiffness properties for this configuration. The microstructure of the RVE configuration for increasing  $(D/H)$  ratio is shown in the Figure 5.10 in which diameter of the fiber has been kept constant.

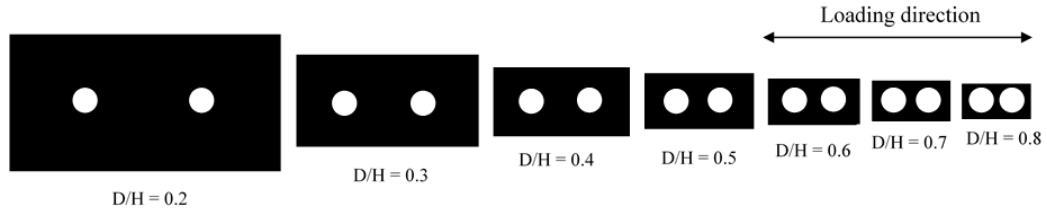


Figure 5.10: Micro-structure of 2IL RVE configuration for different  $(D/H)$  ratios

Similar to the previous configuration, dimensions of the RVE for  $(D/H)$  ratio varying from 0.2 to 0.8 has been calculated using the Eq. 5.1 and stated in the Table 5.3.

Table 5.3: Dimensions of 2IL RVE configuration for different  $(D/H)$  ratio  
(all the dimensions are in  $\mu m$ )

$(D/H)$	Height ( $H$ )	width ( $L$ )	Distance between center of fibers	Volume fraction ( $V_f$ )
0.2	37.5	75	37.5	0.031
0.3	25	50	25	0.00706
0.4	18.75	37.5	18.75	0.126
0.5	15	30	15	0.196
0.6	12.5	25	12.5	0.282
0.7	10.72	21.43	10.72	0.384
0.8	9.375	18.75	9.375	0.502

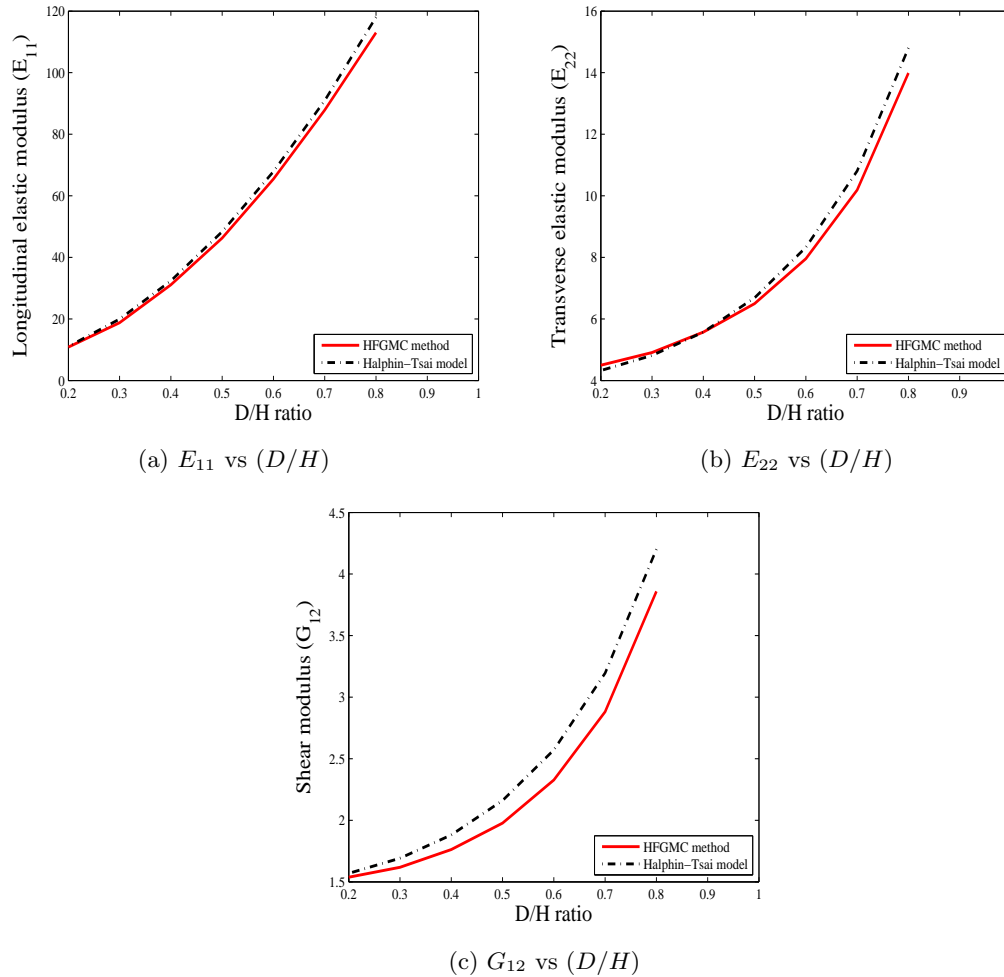


Figure 5.11: Variation in the stiffness properties with increasing  $(D/H)$  ratio for 2IL RVE configuration

The variation in the stiffness properties calculated using HFGMC method and Halpin-Tsai model with increasing  $(D/H)$  ratio is shown in the Figure 5.11. Interaction effect becomes considerable when  $(D/H)$  ratio reaches to 0.5. The longitudinal and transverse elastic modulus calculated using HFGMC method are in agreement with the Halphi-Tsai model results as observed from Figure 5.11a and Figure 5.11b. Minimum RVE size for 2IL configuration by considering the 5 % variation in the stiffness properties obtained using HFGMC results w.r.t. analytical results is observed for  $(D/H) = 0.4$ .

### 5.2.4 2I RVE configuration

2I RVE configuration consists of an  $2 \times 2$  array of fiber elements as described in the Figure 5.3. Dimensions of this configuration has been calculated using the Eq. 5.1 and stated in the Table 5.4. Micro-structure for the 2I configuration for various  $(D/H)$  ratio is shown in the Figure 5.12. Model has been studied to find the minimum RVE size for which near fiber interaction effect is negligible.

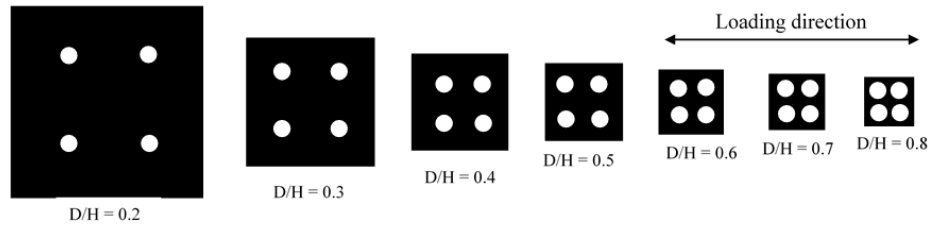


Figure 5.12: Micro-structure for different  $(D/H)$  ratios for 2I RVE configuration

Table 5.4: Dimensions of 2I RVE configuration for different  $(D/H)$  ratio  
(all the dimensions are in  $\mu m$ )

$(D/H)$	Height ( $H$ )	width ( $L$ )	Distance between center of fibers	Volume fraction ( $V_f$ )
0.2	75	75	37.5	0.031
0.3	50	50	25	0.00706
0.4	37.5	37.5	18.75	0.126
0.5	30	30	15	0.196
0.6	25	25	12.5	0.282
0.7	21.43	21.43	10.72	0.384
0.8	18.75	18.75	9.375	0.502

Variation of the stiffness properties w.r.t.  $(D/H)$  ratio changing from 0.2 to 0.8 using HFGMC method and Halphin-Tsai model is shown in the Figure 5.13. These two methods present exact matching results for shear modulus ( $G_{12}$ ) as shown in the Figure 5.7c whereas longitudinal elastic modulus ( $E_{22}$ ) obtained using HFGMC is also closely matches with the analytical results as observed from Figure 5.13a. Considering the 5 % variation in transverse elastic modulus ( $E_{22}$ ) when compared with Halphin-Tsai model results, minimum RVE size for present configuration is observed for  $(D/H) = 0.5$  as fiber interaction effect is negligible for  $(D/H) = 0.5$  or less.

After observing all the RVE configurations presented using the Figure 5.3, for 2I RVE configuration, minimum RVE size is obtained for highest  $(D/H)$  ratio whereas for 2IT configuration, it is observed for lowest  $(D/H)$  ratio. Numerical results formulated using high fidelity generalized method of cells are utmost accordance with the analytical results acquired using Halphin-Tsai model for 2IL and 2I RVE configuration. Next, stiffness properties obtained using HFGMC method for different RVE

configurations has been compared to find the most appropriate configuration to avoid early matrix failure when stacked under tensile loading.

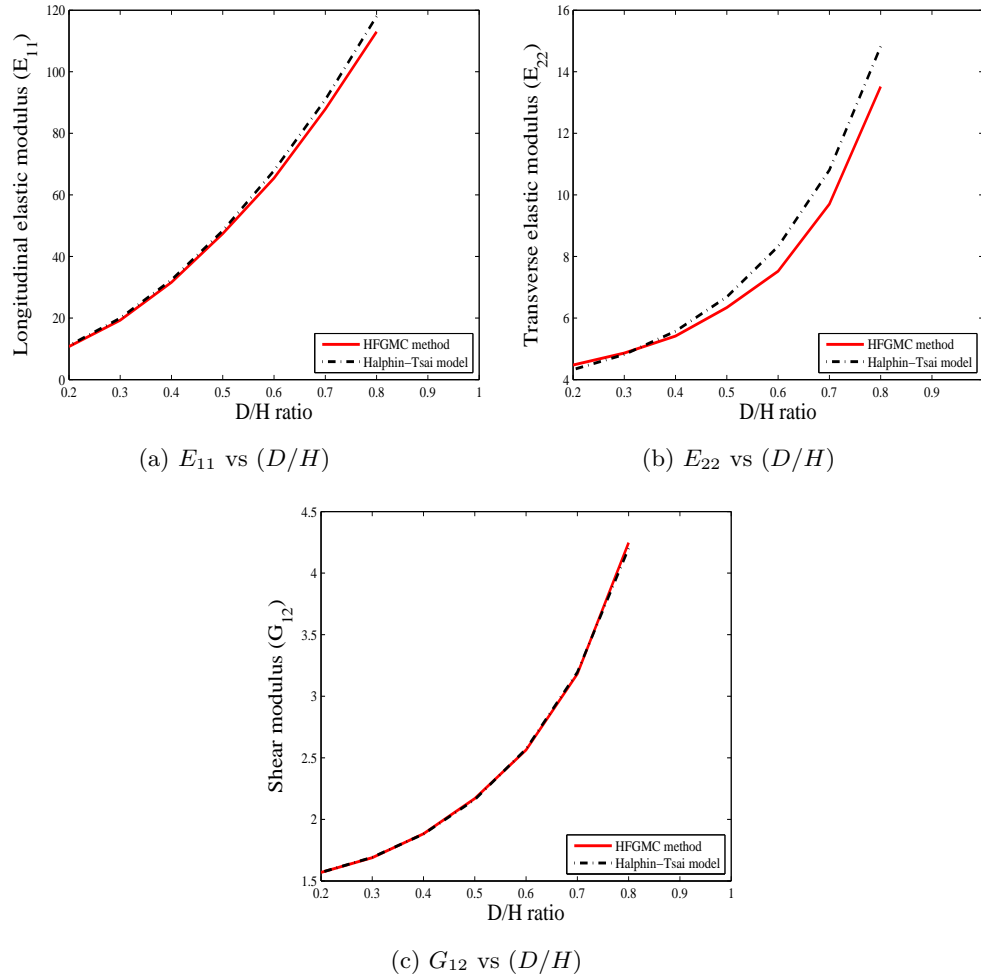


Figure 5.13: Variation in the stiffness properties with increasing  $(D/H)$  ratio for 2I RVE configuration

### 5.3 Comparison Between Different RUC Configurations

RUC configurations described in the Figure 5.3 has been studied to find the most appropriate configuration for micro-mechanical analysis CFRP composites by comparing the stiffness properties ( $E_{11}, E_{22}, G_{12}$ ) of them. In the Figure 5.14, longitudinal elastic modulus of the CFRP composites in the fiber direction has been plotted against varying  $(D/H)$  ratio for all the RVE configurations mentioned in the Figure 5.3 which shows that the longitudinal elastic modulus ( $E_{11}$ ) predicted by all the RVE configurations is same. Therefore, for determining the material properties in the direction

of fiber, any configuration amongst various RVE configurations shown in the Figure 5.3 can be used. Figure 5.15a and 5.15b explains the behavior of transverse elastic modulus ( $E_{22}$ ) and shear modulus ( $G_{12}$ ) respectively w.r.t. increasing ( $D/H$ ) ratio for different RVE configurations. From Figure 5.15a and 5.15b, it can be easily concluded that the results obtained for 1I and 2I configuration are exactly matching whereas 2IT configuration gives maximum values for the effective stiffness properties. The shear modulus for 2IL configuration is the lowest amongst all configurations whereas transverse elastic properties of the CFRP composite are lowest for 1I and 2I configuration. Therefore, 2IT configuration shows higher effective stiffness properties when compared with all other configurations.

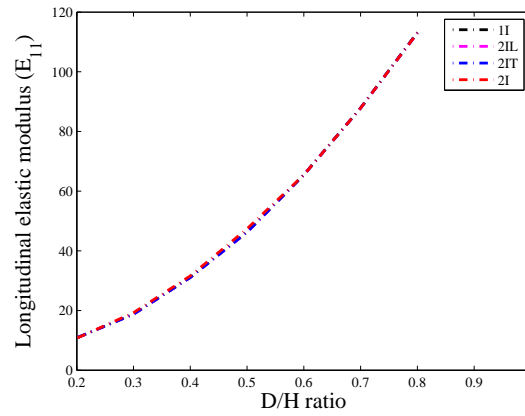


Figure 5.14: Longitudinal elastic modulus ( $E_{11}$ ) for different RVE configurations

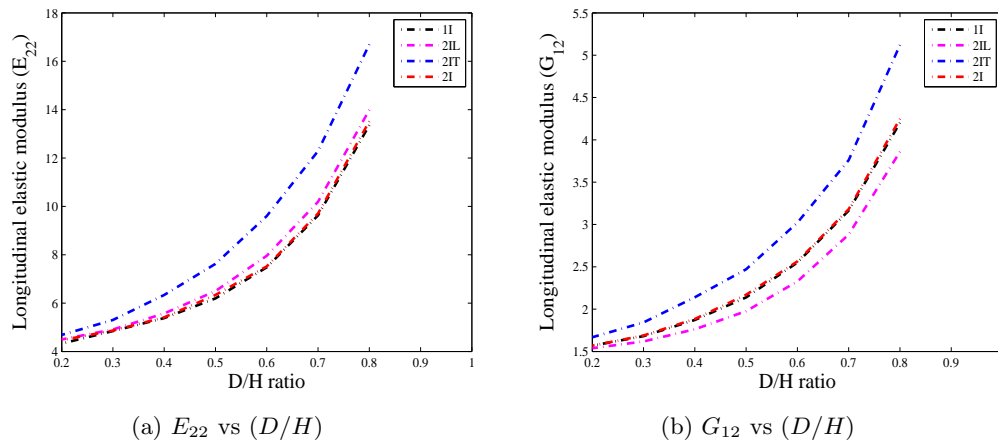


Figure 5.15: Transverse elastic modulus ( $E_{22}$ ) and shear modulus ( $G_{12}$ ) for different RVE configurations



## 5.4 Summary

Different RVE configurations have been analyzed to find minimum RVE size for each configuration to avoid fiber interaction effect. These configurations have been compared for same diameter and volume fraction of the fiber but for varying ( $D/H$ ) ratio. Minimum RVE size is obtained for each configuration by allowing 5% variation w.r.t. analytical results calculated using Halpin-Tsai model. Different configurations shown in the Figure 5.3 has been compared to find the most appropriate model for analyzing the CFRP laminate by considering the interaction effect.

## Chapter 6

# Conclusions and Scope of Future Work

### 6.1 Conclusions

Carbon fiber reinforced polymer composite material exhibits linear and transversely isotropic behavior only till damage initiation point. Once the first trace of damage is initiated, CFRP laminate shows nonlinear and anisotropic nature. The damage progression with increasing strain has been studied thoroughly. The final failure strain for CFRP composite is also realized. Stiffness properties remain constant till failure initiation but after that, they start decreasing gradually. At final failure point, sudden drop is observed for all the stiffness properties except longitudinal elastic modulus ( $E_{11}$ ).

The minimum representative volume element size has been located using same approach for different RVE configurations. To calculate minimum RVE size, various RVE configuration were studied for increasing ( $\frac{D}{H}$ ) ratio from 0.2 to 0.8. By comparing different RVE configurations, it is observed that 2IT configuration carries the highest stiffness properties amongst all for same diameter and volume fraction of the fiber element.

### 6.2 Scope for Future Work

The MATLAB code developed during this project work can be extended to study the constitutive behavior of viscoelastic composites. The same code can be used to study the behavior of more realistic CFRP composites which consists of non-uniformly distributed fiber elements. Constitutive behavior of CFRP composites can also be studied for shear loading using exactly same study with appropriate input conditions. The present micromechanical analysis approach can be further extended to study the behavior of composites under fatigue loading. Same code with small modification can be used to

study the behavior of anisotropic material considering continuous, gradual or exponential degradation also.

# Appendices

# Appendix A

## High Fidelity Generalized Method of Cells (HFGMC)

### A.1 Equation of stress

Total stress for each sub-cell can be calculated using the Eq. 2.6 given below[3, 23]:

$$\sigma^{(\beta\gamma)} = \bar{\sigma}^{(\beta\gamma)} + \sigma_{(10)}^{(\beta\gamma)} y_2^{(\beta)} + \sigma_{(01)}^{(\beta\gamma)} y_3^{(\gamma)} \quad (\text{A.1})$$

Where,  $\bar{\sigma}^{(\beta\gamma)}$  can be calculated using following expression:

$$\bar{\sigma}^{(\beta\gamma)} = C^{(\beta\gamma)} \bar{\epsilon} + C^{(\beta\gamma)} P_{(10)} W_{(10)}^{(\beta\gamma)} + C^{(\beta\gamma)} P_{(01)} W_{(01)}^{(\beta\gamma)}$$

$\sigma_{(10)}$  and  $\sigma_{(01)}$  components used in Eq. A.1 can be obtained using stress moment equation as follows:

$$S_{(mn)}^{(\beta\gamma)} = \frac{1}{h_\beta} \frac{1}{l_\gamma} \int_{-\frac{h_\beta}{2}}^{\frac{h_\beta}{2}} \int_{-\frac{l_\gamma}{2}}^{\frac{l_\gamma}{2}} \sigma^{(\beta\gamma)} y_2^{(\beta)m} y_3^{(\gamma)n} dy_2^{(\beta)} dy_3^{(\gamma)} \quad (\text{A.2})$$

By putting  $m = 1$  and  $n = 0$ , we can calculate the  $S_{(10)}^{(\beta\gamma)}$  component,

$$S_{(10)}^{(\beta\gamma)} = \frac{1}{h_\beta} \frac{1}{l_\gamma} \int_{-\frac{h_\beta}{2}}^{\frac{h_\beta}{2}} \int_{-\frac{l_\gamma}{2}}^{\frac{l_\gamma}{2}} \sigma^{(\beta\gamma)} y_2^{(\beta)1} y_3^{(\gamma)0} dy_2^{(\beta)} dy_3^{(\gamma)}$$

After simplifying and putting Eq. A.1 in Eq. A.2.

$$S_{(10)}^{(\beta\gamma)} = \frac{1}{h_\beta} \frac{1}{l_\gamma} \int_{-\frac{h_\beta}{2}}^{\frac{h_\beta}{2}} \int_{-\frac{l_\gamma}{2}}^{\frac{l_\gamma}{2}} \left( \bar{\sigma}^{(\beta\gamma)} + \sigma_{(10)}^{(\beta\gamma)} y_2^{(\beta)} + \sigma_{(01)}^{(\beta\gamma)} y_3^{(\gamma)} \right) y_2^{(\beta)} dy_2^{(\beta)} dy_3^{(\gamma)}$$

After integrating w.r.t.  $dy_3^{(\gamma)}$  and putting the limits,

$$S_{(10)}^{(\beta\gamma)} = \frac{1}{h_\beta} \int_{-\frac{h_\beta}{2}}^{\frac{h_\beta}{2}} \left[ \bar{\sigma}^{(\beta\gamma)} y_2^{(\beta)} + \sigma_{(10)}^{(\beta\gamma)} y_2^{2(\beta)} \right] dy_2^{(\beta)}$$

Now integrating w.r.t.  $dy_2^{(\beta)}$  and putting the limits.

$$\sigma_{(10)}^{(\beta\gamma)} = \frac{12}{h_\beta^2} S_{(10)}^{(\beta\gamma)}$$

Similarly, by putting  $m = 0$  and  $n = 1$  in the Eq. A.2 and solving,  $\sigma_{(01)}^{(\beta\gamma)}$  can be obtained.

$$\sigma_{(01)}^{(\beta\gamma)} = \frac{12}{l_\gamma^2} S_{(01)}^{(\beta\gamma)} \quad (\text{A.3})$$

Therefore,  $\sigma_{(01)}^{(\beta\gamma)}$  and  $\sigma_{(10)}^{(\beta\gamma)}$  components can be acquired using following expressions:

$$\sigma_{(10)}^{(\beta\gamma)} = \frac{12}{h_\beta^2} S_{(10)}^{(\beta\gamma)} \quad \sigma_{(01)}^{(\beta\gamma)} = \frac{12}{l_\gamma^2} S_{(01)}^{(\beta\gamma)}$$

## A.2 Displacement and traction continuity conditions

The displacement and traction boundary conditions are applied on the surface 1 and surface 2 which are represented by red and green color in the Figure A.1 respectively . RUC is a periodic structure therefore, continuity conditions are applied only on two surfaces.

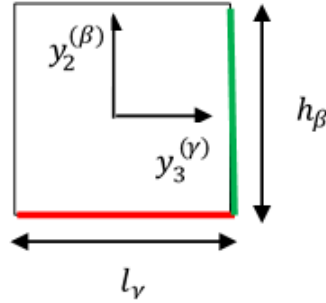


Figure A.1: Sub-cell

### Displacement boundary condition: -

Now, only two surfaces as shown in fig. A.1 has been considered and symmetrical boundary conditions has been assumed.

The displacement continuity equation for surface 1 is,

$$\int_{-\frac{h_\beta}{2}}^{\frac{h_\beta}{2}} \left[ u^{(\beta\gamma)} \Big|_{y_3^{(\gamma)} = \frac{l_\gamma}{2}} - u^{(\beta\gamma_1)} \Big|_{y_3^{(\gamma_1)} = \frac{l_{\gamma_1}}{2}} \right] dy_2^{(\beta)} = 0 \quad (\text{A.4})$$

Using displacement equation 2.1,

$$u^{(\beta\gamma)} \Big|_{y_3^{(\gamma)} = \frac{l_\gamma}{2}} = \bar{\epsilon} \cdot X + W_{(00)}^{(\beta\gamma)} + y_2^{(\beta)} W_{(10)}^{(\beta\gamma)} + \frac{l_\gamma}{2} W_{(01)}^{(\beta\gamma)} + \frac{1}{2} \left( 3y_2^{(\beta)2} - \frac{h_\beta^2}{4} \right) W_{(20)}^{(\beta\gamma)} + \frac{l_\gamma^2}{4} W_{(02)}^{(\beta\gamma)}$$

$$u^{(\beta\gamma_1)}\Big|_{y_3^{(\gamma)}=\frac{l_{\gamma_1}}{2}} = \bar{\epsilon}.X + W_{(00)}^{(\beta\gamma_1)} + y_2^{(\beta)}W_{(10)}^{(\beta\gamma_1)} + \frac{l_{\gamma_1}}{2}W_{(01)}^{(\beta\gamma_1)} + \frac{1}{2}\left(3y_2^{(\beta)2} - \frac{h_\beta^2}{4}\right)W_{(20)}^{(\beta\gamma_1)} + \frac{l_{\gamma_1}^2}{4}W_{(02)}^{(\beta\gamma_1)}$$

By substituting these values in displacement continuity eq. A.4

$$\begin{aligned} I = & \int_{-\frac{h_\beta}{2}}^{\frac{h_\beta}{2}} \left[ \bar{\epsilon}.X + W_{(00)}^{(\beta\gamma)} + y_2^{(\beta)}W_{(10)}^{(\beta\gamma)} + \frac{l_\gamma}{2}W_{(01)}^{(\beta\gamma)} + \frac{1}{2}\left(3y_2^{(\beta)2} - \frac{h_\beta^2}{4}\right)W_{(20)}^{(\beta\gamma)} + \frac{l_{\gamma^2}}{4}W_{(02)}^{(\beta\gamma)} \right] \\ & + \left[ \bar{\epsilon}.X + W_{(00)}^{(\beta\gamma_1)} + y_2^{(\beta)}W_{(10)}^{(\beta\gamma_1)} + \frac{l_{\gamma_1}}{2}W_{(01)}^{(\beta\gamma_1)} + \frac{1}{2}\left(3y_2^{(\beta)2} - \frac{h_\beta^2}{4}\right)W_{(20)}^{(\beta\gamma_1)} + \frac{l_{\gamma_1^2}}{4}W_{(02)}^{(\beta\gamma_1)} \right] dy_3 = 0 \end{aligned}$$

After integrating the above equation and putting the limits,

$$\left[ \Delta W_{(00)}^{(\beta\gamma)} + \frac{l_\gamma}{2}\Delta W_{(01)}^{(\beta\gamma)} + \frac{l_{\gamma^2}}{4}\Delta W_{(02)}^{(\beta\gamma)} \right] - \left[ \Delta W_{(00)}^{(\beta\gamma_1)} - \frac{l_{\gamma_1}}{2}\Delta W_{(01)}^{(\beta\gamma_1)} + \frac{l_{\gamma_1^2}}{4}\Delta W_{(02)}^{(\beta\gamma_1)} \right] = 0 \quad (\text{A.5})$$

This is the final expression for displacement boundary condition on surface 1.

The expression for displacement continuity condition on surface 2 is as follows:

$$\int_{-\frac{l_\gamma}{2}}^{\frac{l_\gamma}{2}} \left[ u^{(\beta\gamma)}\Big|_{y_2^{(\beta)}=\frac{h_\beta}{2}} - u^{(\beta_1\gamma)}\Big|_{y_2^{(\beta_1)}=\frac{h_{\beta_1}}{2}} \right] dy_3^{(\gamma)} = 0 \quad (\text{A.6})$$

By solving eq. A.6,

$$\left[ \Delta W_{(00)}^{(\beta\gamma)} - \frac{h_\beta}{2}\Delta W_{(10)}^{(\beta\gamma)} + \frac{h_{\beta^2}}{4}\Delta W_{(20)}^{(\beta\gamma)} \right] - \left[ \Delta W_{(00)}^{(\beta_1\gamma)} + \frac{h_{\beta_1}}{2}\Delta W_{(10)}^{(\beta_1\gamma)} + \frac{h_{\beta_1^2}}{4}\Delta W_{(20)}^{(\beta_1\gamma)} \right] = 0 \quad (\text{A.7})$$

This is the final expression for displacement boundary condition on surface 2.

### Traction Boundary Condition:-

Now, by considering the traction boundary condition on surface 1,

$$\int_{-\frac{h_\beta}{2}}^{\frac{h_\beta}{2}} \left[ L_3\sigma^{(\beta\gamma)}\Big|_{y_3^{(\gamma)}=-\frac{l_\gamma}{2}} - L_3\sigma^{(\beta\gamma_1)}\Big|_{y_3^{(\gamma_1)}=-\frac{l_{\gamma_1}}{2}} \right] dy_2^{(\beta)} = 0 \quad (\text{A.8})$$

$$L_3\sigma^{(\beta\gamma)}\Big|_{y_3^{(\gamma)}} = \left[ L_3\bar{\sigma}^{(\beta\gamma)} + L_3\sigma_{(10)}^{(\beta\gamma)}y_2^{(\beta)} + L_3\sigma_{(01)}^{(\beta\gamma)}y_3^{(\gamma)} \right]$$

Put eq. 2.6 in eq. A.8.

$$L_3 \sigma^{(\beta\gamma)} \Big|_{y_3^{(\gamma)} = \frac{-l_\gamma}{2}} = C^{(\beta\gamma)} \bar{\epsilon} L_3 + C_{(\beta\gamma)} P_{(10)} W_{(10)}^{(\beta\gamma)} L_3 + C_{(\beta\gamma)} P_{(01)} W_{(01)}^{(\beta\gamma)} L_3 + C_{(\beta\gamma)} P_{(20)} W_{(20)}^{(\beta\gamma)} y_2^{(\beta)} L_3 \\ + C_{(\beta\gamma)} P_{(02)} W_{(02)}^{(\beta\gamma)} y_3^{(\gamma)} L_3$$

$$L_3 \sigma^{(\beta\gamma_1)} \Big|_{y_3^{(\gamma_1)} = \frac{-l_{\gamma_1}}{2}} = C^{(\beta\gamma_1)} \bar{\epsilon} L_3 + C_{(\beta\gamma_1)} P_{(10)} W_{(10)}^{(\beta\gamma_1)} L_3 + C_{(\beta\gamma_1)} P_{(01)} W_{(01)}^{(\beta\gamma_1)} L_3 + C_{(\beta\gamma_1)} P_{(20)} W_{(20)}^{(\beta\gamma_1)} y_2^{(\beta)} L_3 \\ + C_{(\beta\gamma_1)} P_{(02)} W_{(02)}^{(\beta\gamma_1)} y_3^{(\gamma_1)} L_3$$

Putting these values in the traction continuity eq. A.8,

$$I = \int_{\frac{-h_\beta}{2}}^{\frac{h_\beta}{2}} \left[ C^{(\beta\gamma)} \bar{\epsilon} L_3 + C_{(\beta\gamma)} P_{(10)} W_{(10)}^{(\beta\gamma)} L_3 + C_{(\beta\gamma)} P_{(01)} W_{(01)}^{(\beta\gamma)} L_3 + C_{(\beta\gamma)} P_{(20)} W_{(20)}^{(\beta\gamma)} y_2^{(\beta)} L_3 \right] \\ \left[ + C_{(\beta\gamma)} P_{(02)} W_{(02)}^{(\beta\gamma)} y_3^{(\gamma)} L_3 - C^{(\beta\gamma_1)} \bar{\epsilon} L_3 - C_{(\beta\gamma_1)} P_{(10)} W_{(10)}^{(\beta\gamma_1)} L_3 - C_{(\beta\gamma_1)} P_{(01)} W_{(01)}^{(\beta\gamma_1)} L_3 \right] \\ \left[ - C_{(\beta\gamma_1)} P_{(20)} W_{(20)}^{(\beta\gamma_1)} y_2^{(\beta)} L_3 - C_{(\beta\gamma_1)} P_{(02)} W_{(02)}^{(\beta\gamma_1)} y_3^{(\gamma_1)} L_3 \right] dy_2^{(\beta)} = 0$$

By solving the above expression,

$$\left[ A_{3(00)}^{(\beta\gamma_1)} - A_{3(00)}^{(\beta\gamma)} \right] \Delta \bar{\epsilon} = \left[ A_{3(10)}^{(\beta\gamma)} \Delta W_{(10)}^{(\beta\gamma)} + A_{3(01)}^{(\beta\gamma)} \Delta W_{(01)}^{(\beta\gamma)} + \frac{l_\gamma}{2} A_{3(02)}^{(\beta\gamma)} \Delta W_{(02)}^{(\beta\gamma)} \right] \\ - \left[ A_{3(10)}^{(\beta\gamma_1)} \Delta W_{(10)}^{(\beta\gamma_1)} + A_{3(01)}^{(\beta\gamma_1)} \Delta W_{(01)}^{(\beta\gamma_1)} + \frac{l_{\gamma_1}}{2} A_{3(02)}^{(\beta\gamma_1)} \Delta W_{(02)}^{(\beta\gamma_1)} \right] \quad (\text{A.9})$$

This is the final expression for traction continuity on surface 1.

Similarly, when displacement and traction boundary conditions has been applied on surface 2,

$$\int_{\frac{-l_\gamma}{2}}^{\frac{l_\gamma}{2}} \left[ L_2 \sigma^{(\beta\gamma)} \Big|_{y_2^{(\beta)} = -\frac{h_\beta}{2}} - L_2 \sigma^{(\beta_1\gamma)} \Big|_{y_2^{(\beta_1)} = -\frac{h_{\beta_1}}{2}} \right] dy_3^{(\gamma)} = 0 \quad (\text{A.10})$$

By solving this expression,

$$\left[ A_{2(00)}^{(\beta_1\gamma)} - A_{2(00)}^{(\beta\gamma)} \right] \Delta \bar{\epsilon} = \left[ A_{2(10)}^{(\beta\gamma)} \Delta W_{(10)}^{(\beta\gamma)} + A_{2(01)}^{(\beta\gamma)} \Delta W_{(01)}^{(\beta\gamma)} - \frac{h_\beta}{2} A_{2(20)}^{(\beta\gamma)} \Delta W_{(20)}^{(\beta\gamma)} \right] \\ - \left[ A_{2(10)}^{(\beta_1\gamma)} \Delta W_{(10)}^{(\beta_1\gamma)} + A_{2(01)}^{(\beta_1\gamma)} \Delta W_{(01)}^{(\beta_1\gamma)} + \frac{h_{\beta_1}}{2} A_{2(20)}^{(\beta_1\gamma)} \Delta W_{(20)}^{(\beta_1\gamma)} \right] \quad (\text{A.11})$$



### A.3 Residual vector

The residual vector can be calculated using following expression for each sub-cell,

$$R^{(\beta\gamma)} = \begin{bmatrix} \int [L_2\sigma^{(\beta\gamma)} - L_2\sigma^{(\beta_1\gamma)}] dy_3^{(\gamma)} \\ \int [L_3\sigma^{(\beta\gamma)} - L_3\sigma^{(\beta\gamma_1)}] dy_2^{(\beta)} \\ L_2\sigma_{(10)}^{(\beta\gamma)} - L_3\sigma_{(01)}^{(\beta\gamma)} \\ 0 \\ 0 \end{bmatrix} = \begin{bmatrix} [L_2\sigma^{(\beta\gamma)_1} - L_2\sigma^{(\beta_1\gamma)_3}] \\ [L_3\sigma^{(\beta\gamma)_2} - L_3\sigma^{(\beta\gamma_1)_4}] \\ L_2\sigma_{(10)}^{(\beta\gamma)} - L_3\sigma_{(01)}^{(\beta\gamma)} \\ 0 \\ 0 \end{bmatrix} \quad (\text{A.12})$$

As seen in the Figure. A.2, there are four integration points numbered 1,2,3 and 4 has been considered in each sub-cell.

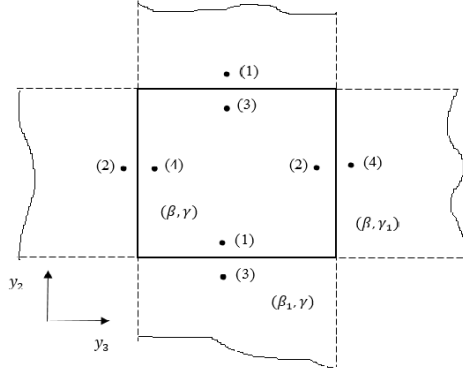


Figure A.2: Integration points on sub-cell

By considering, stress expression for each sub-cell.

$$\sigma^{(\beta\gamma)} = \bar{\sigma}^{(\beta\gamma)} + \sigma_{(10)}^{(\beta\gamma)} y_2^{(\beta)} + \sigma_{(01)}^{(\beta\gamma)} y_3^{(\gamma)} \quad (\text{A.13})$$

Equilibrium condition has been satisfied only inside the sub-cell. Now let's calculate stress acting at point 1, inside the sub-cell.

$$\sigma^{(\beta\gamma)_1} = \bar{\sigma}^{(\beta\gamma)} + \sigma_{(10)}^{(\beta\gamma)} y_2^{(\beta)} + \sigma_{(01)}^{(\beta\gamma)} y_3^{(\gamma)}$$

Co-ordinates of the point 1 are  $\left(-\frac{h_\beta}{2}, 0\right)$

Putting this value into eq. A.13,

$$\sigma^{(\beta\gamma)_1} = \bar{\sigma}^{(\beta\gamma)} - \left(\frac{h_\beta}{2}\right) \sigma_{(10)}^{(\beta\gamma)} \quad (\text{A.14})$$

Now the stress expression at point 3 is

$$\sigma^{(\beta\gamma)_3} = \bar{\sigma}^{(\beta\gamma)} + \sigma_{(10)}^{(\beta\gamma)} y_2^{(\beta)} + \sigma_{(01)}^{(\beta\gamma)} y_3^{(\gamma)}$$

The co-ordinates of point 3 are  $\left(\frac{h_\beta}{2}, 0\right)$

Putting this value into eq. A.13,

$$\sigma^{(\beta\gamma)_3} = \bar{\sigma}^{(\beta\gamma)} + \left(\frac{h_\beta}{2}\right) \sigma_{(10)}^{(\beta\gamma)} \quad (\text{A.15})$$

By solving eq. A.14 and eq. A.15, we can get

$$\sigma_{(10)}^{(\beta\gamma)} = \frac{1}{h_\beta} \left( \sigma^{(\beta\gamma)_3} - \sigma^{(\beta\gamma)_1} \right)$$

Similarly we can calculate total stress at point 2 and 4 which are located at  $y_2^{(\beta)} = 0$  and  $y_3^{(\gamma)} = \pm \frac{l_\gamma}{2}$  respectively.

$$\sigma^{(\beta\gamma)_2} = \bar{\sigma}^{(\beta\gamma)} + \sigma_{(01)}^{(\beta\gamma)} \left( \frac{l_\gamma}{2} \right)$$

$$\sigma^{(\beta\gamma)_4} = \bar{\sigma}^{(\beta\gamma)} - \sigma_{(01)}^{(\beta\gamma)} \left( \frac{l_\gamma}{2} \right)$$

By solving these equations,

$$\sigma_{(01)}^{(\beta\gamma)} = \frac{1}{l_\gamma} \left( \sigma^{(\beta\gamma)_2} - \sigma^{(\beta\gamma)_4} \right)$$

Hence, higher order stresses can be calculated at integration points.

# References

- [1] Brunel university Mohanty, Grow2Build. 2009. [ix](#), [2](#)
- [2] Ivancevic D. and Smojver I. Micromechanical damage modelling using a two-scale method for laminated composite structures. *Composite Structures*, 108:223–233, 2014. [ix](#), [4](#), [9](#), [10](#), [20](#), [33](#)
- [3] Haj-Ali R. and Aboudi J. Nonlinear micromechanical formulation of the high fidelity generalized method of cells. *International Journal of Solids and Structures*, 46:2577–2592, 2009. [ix](#), [3](#), [4](#), [5](#), [6](#), [7](#), [9](#), [11](#), [12](#), [15](#), [22](#), [63](#)
- [4] Jones R. *Mechanics of composite materials*. Taylor and francis, 1999. [xi](#), [2](#), [3](#), [4](#), [5](#), [25](#), [34](#)
- [5] Mohammad Kashfuddoja. *Experimental and Numerical Study of Composite Patch Repair on Open Hole Carbon Fiber Reinforced Polymer Panel under Tensile Loading*. PhD thesis, Indian Institute of Technology,Hyderabad, 2014. [xi](#), [30](#), [34](#), [35](#), [45](#)
- [6] Satish K., Harit D., Mohan S., Jung O., and David S. Fiber from polypropylene/nano carbon fiber composites. *Polymer*, 43((2002)):1701–1703, 2002. [3](#), [30](#)
- [7] Kanoute P., Boso D. P., Chaboche J.L., and B.A. Schrefler. Multiscale methods for composites: a review. *Arch Comput Methods Eng*, 16((2009)):31–35, 2009. [4](#), [5](#), [6](#)
- [8] IA Kunin. The theory of elastic media with microstructure and the theory of dislocations. In *Mechanics of generalized continua*, pages 321–329. Springer, 1968. [5](#)
- [9] A Cemal Eringen. Simple microfluids. *International Journal of Engineering Science*, 2(2):205–217, 1964. [5](#)
- [10] E Kröner. Elasticity theory of materials with long range cohesive forces. *International Journal of Solids and Structures*, 3(5):731–742, 1967. [5](#)
- [11] Zdeněk P Bažant. Instability, ductility, and size effect in strain-softening concrete. *Journal of the engineering mechanics division*, 102(2):331–344, 1976. [5](#), [38](#), [39](#)

- [12] JA Krumhansl. Some considerations of the relation between solid state physics and generalized continuum mechanics. In *Mechanics of generalized continua*, pages 298–311. Springer, 1968. [5](#)
- [13] RD Mindlin and HF Tiersten. Effects of couple-stresses in linear elasticity. *Archive for Rational Mechanics and Analysis*, 11(1):415–448, 1962. [5](#)
- [14] Voigt W. ber die beziehung zwischen den beiden elastizittskonstanten isotroper krper. *wied ann.* 38(38):573–587, 1889. [5](#)
- [15] Reuss A. Berechnung del fliessgrenze von mischkristallen auf grund der plastizittbedingung fr einkristalle. *Z Angew Math Mech*, 9(9):49–58, 1929. [5](#)
- [16] J.W. Hutchinson. Bounds and self-consistent estimates for creep of polycrystalline materials. *Proc.R.Soc.Lond.A*, 348(348):101–127, 1976. [6](#)
- [17] G.R. Canova A. Molinari and S. Ahzi. A self consistent approach of the large deformation polycrystal viscoplasticity. *Acta metall*, 35(12):2983–2994, 1987. [6](#)
- [18] Hashin Z. and Shtrikman S. On some variational principles in anisotropic and nonhomogeneous elasticity. *J.Mech.Phys.Solids*, 10(10):335–342, 1962. [6](#), [10](#)
- [19] Hashin Z. and Shtrikman S. A vaiational approach to the theory of the elastic behaviour of polycrystals. *J.Mech.Phys.Solids*, 10(10):343–352, 1962. [6](#), [10](#)
- [20] Hashin Z. and Shtrikman S. A variational approach to the theory of the elastic behavior of multiphase materials. *J.Mech.Phys.Solids*, 11(11):127–140, 1963. [6](#), [10](#)
- [21] T. Mori and K. Tanka. Average stress in matrix and average elastic energy of materials with misfitting inclusions. *Acta Metallurgica*, 21(21):571–574, 1973. [6](#)
- [22] Aboudi J. Micrmechanical analysis of composites by method of cells. *Appl Mech Rev*, vol 42(7):193–221, July 1989. [7](#), [9](#)
- [23] Aboudi J. The generalized method of cells and high-fidelity generalized method of cells micromechanical modelsa review. *Mechanics of Advanced Materials and Structures*, 11(4:5):329–366, 2004. [7](#), [8](#), [12](#), [63](#)
- [24] P. Papanikos K.I. Tserpes and Th. Kermanidis. Progressive fatigue damage modelling of cfrp laminates at the mesoscale level. 2002. [8](#), [9](#), [10](#), [11](#), [24](#), [25](#)

- [25] Shokrieh M. and Lessard L. Progressive fatigue damage modeling of composite materials, part i: modeling. *Journal of Composite Materials*, 2000. 8, 9, 10, 24, 25, 28
- [26] Sourabh K., Viswanath C., Mahendrakumar M., and Ramji M. Progressive failure analysis of cfrp laminate with interacting holes under compressive loading. *Journal of Composite Materials*, 0:1–21, 2014. 8, 9, 10, 24, 25
- [27] W.J. Drugan and J.R. Willis. A micro-mechanics based nonlocal constitutive equation and estimates of representative volume element size for elastic composites. *J.Mech.Phys.Solids*, 44(4):497–524, 1996. 8, 9, 10, 50
- [28] W.J. Drugan and J.R. Willis. Micro-mechanics based variational estimates for a higher-order nonlocal constitutive equation and optimal choice of effective moduli for elastic composites. *J.Mech.Phys.Solids*, 48(48):1359–1387, 2000. 8, 9, 10, 50
- [29] W.J. Drugan. Two exact micromechanics-based nonlocal constitutive equations for random linear elastic composite materials. *J.Mech.Phys.Solids*, 51(51):1745–1772, 2003. 8, 10
- [30] Paley M. and Aboudi J. Micromechanical analysis of composites by the generalized cells model. *Mechanics of Materials*, vol. 14((1992)):127–139, 1992. 8
- [31] Papanikos P. Tserpes K. I., Labeas G. and Kermanidis Th. Strength prediction of bolted joints in graphite/epoxy composite laminates. *Composites: Part B*, volume 33((2002)):521529, 2000. 9, 10, 24, 25, 29
- [32] Shokrieh M. and Lessard L. Progressive fatigue damage modeling of composite materials, part ii: material characterization and model verification. *Journal of Composite Materials*, 34(13/2000):1081–1116, 2000. 9, 10, 24, 28
- [33] Mohammad Kashfuddoja Jabir Ubaid and Manoharan Ramji. Strength prediction and progressive failure analysis of carbon fiber reinforced polymer laminate with multiple interacting holes involving three dimensional finite element analysis and digital image correlation. *International Journal of Damage Mechanics*, 23(5):609–635, 2013. 9, 10, 24, 25
- [34] Aboudi J. Micro-mechanical analysis of thermo-inelastic multi-phase short-fiber composites. *Composites Engineering*, 5(7):839–850, 1995. 9
- [35] Nali P. and Carrera E. A numerical assessment on two-dimensional failure criteria for composite layered structures. *Composites: Part B*, 43((2012)):280–289, 2012. 9, 25, 26

- 
- [36] Steven M and Andrew C. A comparison of multicontinuum theory based failure simulation with experimental results. *Composites Science and Technology*, 64(2004):517–527, 2002. [10](#), [25](#), [26](#), [29](#)
- [37] Hinton M.J., Kaddour A.S., and Soden P.D. *Failure Criteria in Fibre Reinforced Polymer Composites: The World-Wide Failure Exercise*. Elsevier journals, 2014. [24](#), [25](#), [26](#)
- [38] LJ Hart-Smith. Predictions of a generalized maximum-shear-stress failure criterion for certain fibrous composite laminates. *Composites Science and Technology*, 58(7):1179–1208, 1998. [25](#)
- [39] Kuo-Shih Liu and Stephen W Tsai. A progressive quadratic failure criterion for a laminate. *Composites Science and Technology*, 58(7):1023–1032, 1998. [25](#)
- [40] J Steven Mayes and Andrew C Hansen. A comparison of multicontinuum theory based failure simulation with experimental results. *Composites Science and Technology*, 64(3):517–527, 2004. [26](#)